Imperial College London

A Critical Review on Hubble Tension

Author: Zhihan Yuan

Supervisor: João Magueijo

Submitted in partial fulfilment of the requirements for the degree of Master of Science of Imperial College London

22 September 2021

Abstract

The late universe and early universe measurements of the Hubble constant disagree to a non-negligible extent. This problem is often referred to as the Hubble tension. In this paper, we examine various methods of measuring the Hubble constant, including direct measurements using cosmic distance ladder, ΛCDM model fit of cosmic microwave background observations, baryon acoustic oscillations and strong gravitational lensing. We compare different experiments among the two main approaches, the distance ladder method and the cosmic microwave background measurements. We find that the most reliable result from each method found in literature agree up to 1σ. Nevertheless, current understanding of systematic effects cannot account for the discrepancy between these values and those from other experiments. More observations are needed to fully resolve Hubble tension.

Contents

1. INTRODUCTION

Ever since Edwin Hubble astonished the world with his expanding universe theory in 1929, astronomers and cosmologists have been searching for value of the Hubble constant H_0, the proportionality constant in Hubble's law, which states that the radial velocity of nearby galaxies is proportional to their distance from us observers on earth [1]. Figure 1 is the original Hubble diagram from Hubble's 1929 paper, which plots the velocity of an astronomical object with respect to its distance from an observer on earth. The proportional

relation is evident in the linear fit of the data points in the graph. Since the universe is expanding, the objects we are observing through the expanding space appears to be moving away from us. As the radiation from distant objects travels towards us, the wavelength of the radiation increases and will be longer than the emitted wavelength by the time the light reaches the observer. This phenomenon is termed cosmological redshift, described by the redshift parameter z, which will be called redshift for short during the rest of the discussion. To connect the distance of an object to its redshift, we need to find the dependence of velocity on the redshift. Although the proportionality between velocity and distance is quite clear in all cases, the relationship between redshift and velocity is dependent on the cosmological model adopted. For small redshift, however, we have an approximately proportional relationship between velocity and redshift, $v \approx cz$ where v is the velocity, c is the speed of light and z is the redshift [2].

Therefore, at small redshift, we can find the Hubble constant in a model independent way through the relation

$$cz = H_0 d \tag{1}$$

where d is the distance of the object from the observer on earth [3]. The redshift parameter is separately given by

$$z = \frac{\lambda_{observed} - \lambda_{emitted}}{\lambda_{emitted}} \tag{2}$$

where $\lambda_{observed}$ and $\lambda_{emitted}$ are the observed and emitted wavelengths from the object. Redshift is higher for most distant objects due to the expansion of the universe. Eq.(1) allows us to infer the value of the Hubble constant from the measured redshift combined with the distance of the object.

The classical approach to measuring the Hubble constant is to obtain local values of H_0 directly from the astrophysics of celestial objects. Naturally, an important step for this approach is calibrating the distance of celestial objects using the cosmic distance ladder. The distance ladder is the collection of techniques used to determine distance of different scales in the universe. Each step takes us to a greater distance and relies on the previous step for calibration [5].

For nearby stars, we take the first step, stellar parallax, a relatively direct method that only involves simple trigonometry [5]. Using distant stars as the background, we observe a relative shift of a nearby star at different points of the Earth's orbit. With prior knowledge

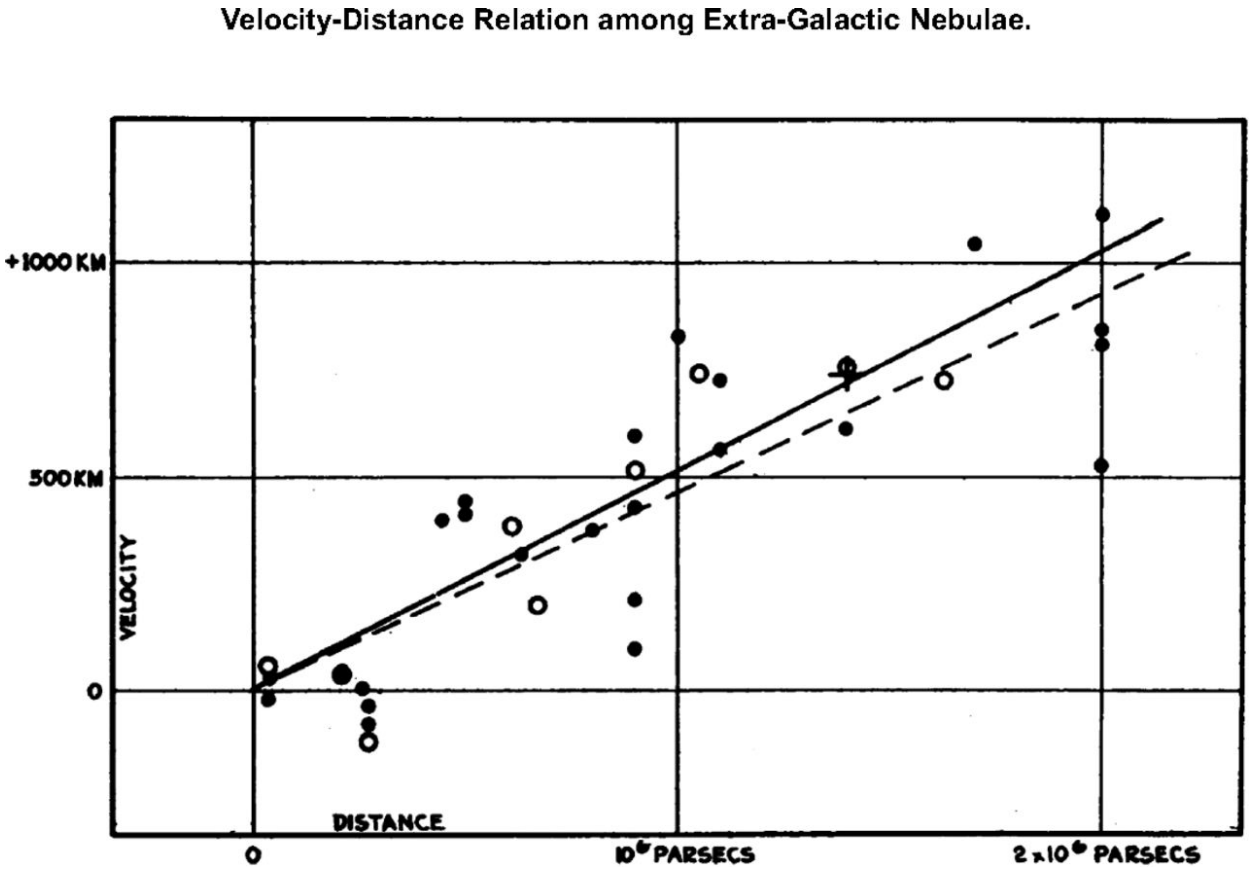

FIG. 1: Plot of radial velocity versus distance for extragalactic nebulae. The vertical axis represents radial velocity in kilometers per second and the horizontal axis represents distance in parsecs. "Radial velocities, corrected for solar motion, are plotted against distances estimated from involved stars and mean luminosities of nebulae in a cluster. The black discs and full line represent the solution for solar motion using the nebulae individually; the circles and broken line represent the solution combining the nebulae into groups; the cross represents the mean velocity corresponding to the mean distance of 22 nebulae whose distances could not be estimated individually" [4].

of the distance between the two points of the Earth's orbit, this shift, known as the parallax angle, in turn gives us the distance to the nearby star. A schematic illustration of the trigonometric stellar parallax method is shown in Figure 2. The angle p labeled in the diagram in Figure 2 is the parallax angle between Earth's position in June and its position in December on its orbit around the Sun.

The second step in the distance ladder relies on standard candles. Standard candles are objects with known absolute brightness determined from other observable properties,

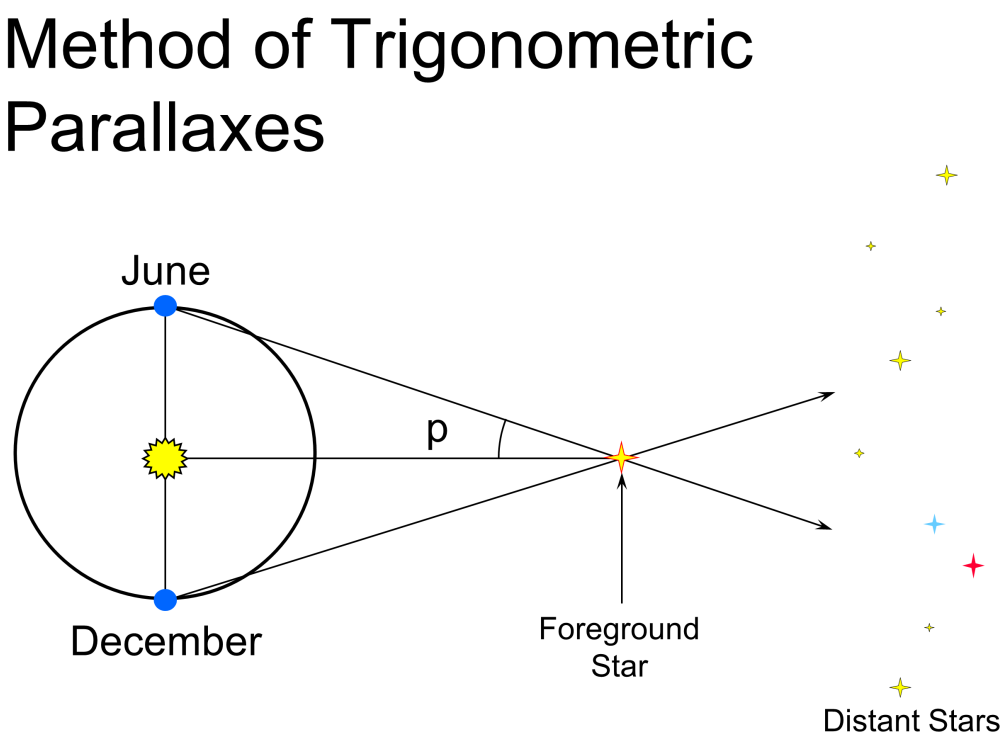

FIG. 2: Schematic Diagram of Stellar Parallax. [6]

so that we can compute the distance by comparing the apparent brightness to the absolute brightness of the object [7]. For more distant stars in the Milky Way and in nearby galaxies, the most commonly used standard candle is the Cepheid variable, a variable star with pulsating luminosity which is related to the oscillation period [8]. Cepheid variables with a longer period are brighter than those with a shorter period. This period-luminosity relation is called Leavitt Law. Figure 3 shows the original plot of the period-luminosity relation from 25 Cepheid variable stars in the Small Magellanic Cloud [9] from Leavitt's paper published in 1912. We can therefore determine the absolute brightness of Cepheid variables by observing the pulsating period and use them as standard candles.

For stars in more distant galaxies, astronomers often use Type Ia supernovae as standard candles. A Type Ia supernova is the explosion of a white dwarf in a binary star system [5]. When the white dwarf accretes matter to a certain limit, it collapses and causes extremely

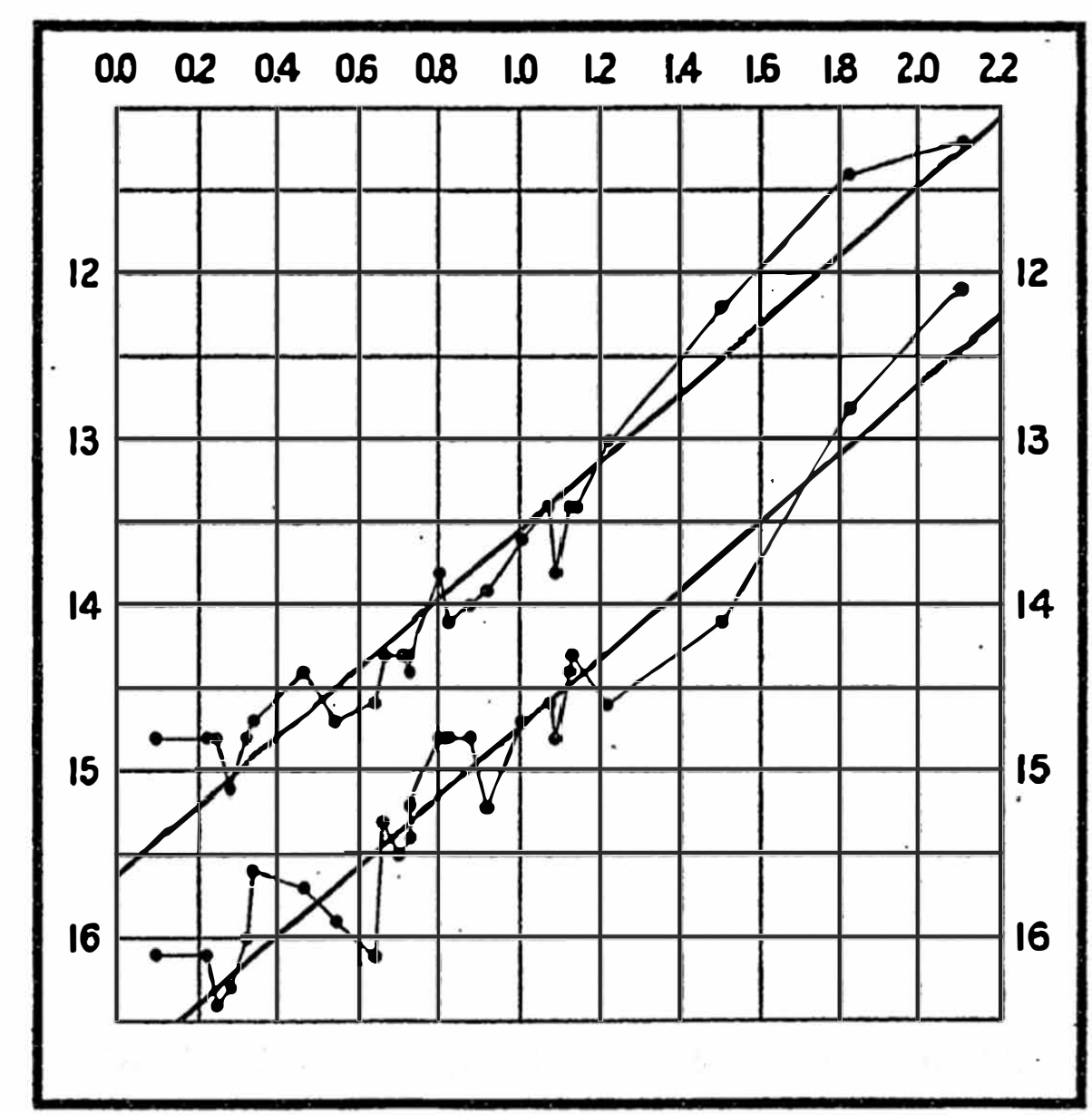

FIG. 3: Plot of the period-luminosity relation of 25 variable stars from Leavitt's 1912 paper. The horizontal axis marks the logarithms of the periods of the variable stars and the vertical axis shows their corresponding apparent magnitude [9].

luminous explosion with a distinctly shaped light curve. The peak luminosity is related to the rate of decay of the light curve, allowing us to determine the relative luminosity among different Type Ia supernovae. As shown in the upper plot in Figure 4, lights curves with higher peak luminosity decays more slowly while those with lower peak luminosity decays

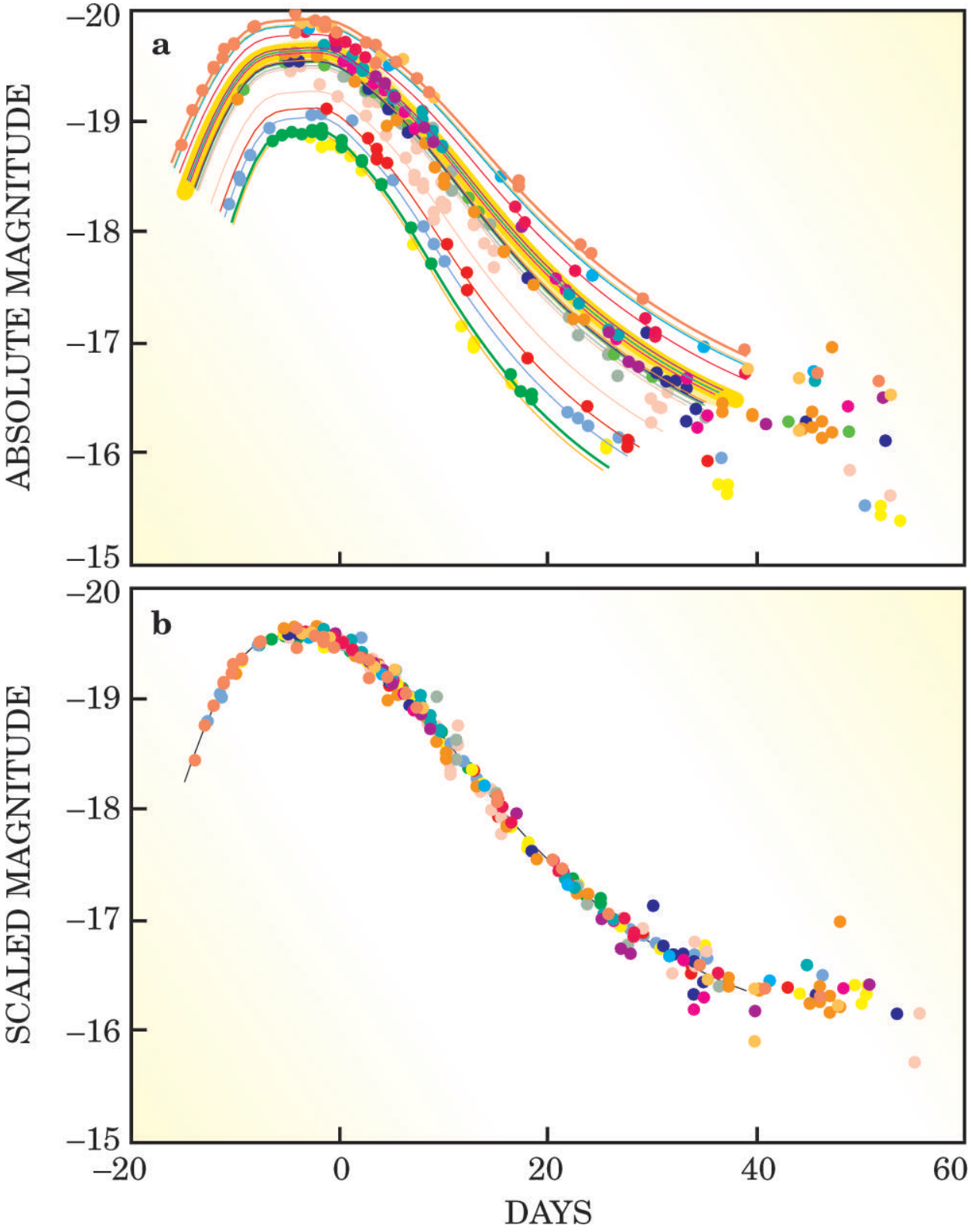

FIG. 4: The upper plot shows the light curves for different Type Ia Supernovae. The decline rate of SNe Ia is associated to its peak brightness. The lower plot shows the SNe Ia light curves standardized by the "stretch method" [10].

faster. After correcting for this luminosity-decay rate relation, also known as the "stretch factor", Type Ia supernovae can be used as standard candles [11]. Using Cepheid variables on the previous step of the distance ladder to determine the absolute distance and luminosity of nearby Type Ia supernovae (SNe Ia), we are able to determine the absolute luminosity of distant SNe Ia and thus move further up on the cosmic distance ladder.

Sometimes the global properties of a galaxy are used to determine luminosity. For spiral galaxies, the luminosity and the rotational velocity follow the Tully-Fisher relation, which allows us to determine the relative distances of different spiral galaxies. Similarly, elliptical galaxies follow the Faber-Jackson relation [7]. Therefore, these galaxies also serve as standard candles.

We will further discuss the conventional distance ladder approach and its variations in Section 2. Aside from the distance ladder method, there are several other relatively indirect ways of measuring the Hubble constant. One major source of constraints on the Hubble constant is observations of the cosmic microwave background (CMB). The Hubble constant is obtained from CMB experiments by fitting the data to the ΛCMD model, which will be introduced later in Section 3.1. The measurement of H_0 from CMB experiments differs from the local value obtained using the distance ladder method. This discrepancy, often referred to as the Hubble tension, is the main theme and motivation of this paper.

Other approaches to the measurement of the Hubble constant include the "inverse distance ladder" method using baryon acoustic oscillations and Type Ia Supernovae, which will be introduced in Section 4. Another way of measuring the Hubble constant is through the "time-delay" method in strong gravitational lensing, which is to be explained in Section 5. In Section 6, we will compare the values of H_0 measured through different methods and analyze the discrepancy between them.

2. LOCAL MEASUREMENTS OF THE HUBBLE CONSTANT

2.1. Cepheid Calibrated Measurements

In the second half of the 20th century, two measurements of the Hubble constant from galaxies lead to a major disagreement. Sandage et al. claimed that $H_0 = 43 \pm 11$ km s^{-1} Mpc^{-1} [12] while de Vaucouleurs et al. found that H_0 was twice this value,

96 ± 10 km s^{-1} Mpc^{-1} [13]. This debate was resolved by the Hubble Space Telescope (HST) key project at the turn of the century, which settled on a value of $H_0 = 72 \pm 8$ km s^{-1} Mpc^{-1} from Cepheid calibrated Type Ia Supernovae, Type II supernovae, the Tully-Fisher relation, the fundamental plane for elliptical galaxies, and surface-brightness fluctuations [14].

The Supernovae, H_0, for the Equation of State of dark energy (SH0ES) project is a major experiment that uses the distance ladder method to measure the Hubble constant. The SH0ES project mainly uses observations of Cepheid variables in the host galaxies of SNe Ia from the HST. In 2011, Riess et al. obtained a value of the Hubble constant with around 3% uncertainty $H_0 = 73.8 \pm 2.4$ km s^{-1} Mpc^{-1}. They calibrated 8 recent SNe Ia using geometric distance to Cepheids in NGC 4285 (a spiral galaxy in the constellation Canes Venatici) calibrated by megamasers, 13 Milky Way Cepheids measured with trigonometric parallaxes, as well as 92 Cepheids in Large Magellanic Cloud (LMC), the distance to which is determined from studies of detached eclipsing binary stars [15, 16]. Then they used these 8 SNe Ia to calibrate the magnitude-redshift of large SNe Ia sample groups [17] that extend into the Hubble flow, where the effects on the velocity of galaxies are dominated by the expansion of the universe.

Careful examination of the Cepheid distance method, however, has lead to findings of potential systematic errors in the measurement. In 2014, Efstathiou performed a reanalysis on the Riess et al. (2011) data and corrected for a skew in the global fits of the period-luminosity relation due to low metallicity Cepheids in the sample. In the next year, Rigault et al. claims that observations of SNe Ia from the Galaxy Evolution Explorer suggested that the Cepheid calibrated SNe Ia from the HST are originated in largely star-forming environments, while only around half the SNe sample in the Hubble flow are found in star-forming environments. Their reanalysis brings down the value of Hubble constant to 70.6 ± 2.6 km s^{-1} Mpc^{-1}, which agrees to the Planck value within around 1σ [18].

Riess et al. examined Efstathiou's correction to their 2011 results in their 2016 paper, where they reduced the uncertainty of the local measurement of the Hubble constant to 2.4% with a best estimate of $H_0 = 73.24 \pm 1.74$ km s^{-1} Mpc^{-1} by increasing the sample of Cepheid calibrated SNe Ia to 19. In addition to Cepheids in the SNe Ia host galaxies used in the former result, the results include Cepheids in the Andromeda Galaxy (M31) calibrated by detached eclipsing binaries (DEBs). They have also taken into account of the reanalysis performed by Efstathiou (2014) and chosen better anchors for determination of the Hubble

constant.

In 2018, the same group decreased the uncertainty of the local measurement of the Hubble constant of by including the new data release from Gaia, a stellar survey led by the European Space Agency that gives precise measurements of hundreds of Milky Way Cepheids, resulting in a slightly different value of $H_0 = 73.52 \pm 1.62$ km s^{-1} Mpc^{-1} [19, 20].

The Riess et al. (2019) results lowered the uncertainty to 1% with new HST observations of 70 Cepheids in the Large Magellanic Cloud, which were measured and analyzed independent from knowledge of the new DEB distance. The period-luminosity relation observed of these 70 Cepheids completes the missing connection between the geometric distance to the LMC measured by DEBs and the luminosity of SNe Ia. Incorporating the improved measurements, they give updated best estimate $H_0 = 74.03 \pm 1.42$ km s^{-1} Mpc^{-1}, pushing the difference between the local value of H_0 and the Planck value to 4.4σ [21]. They also addressed the potential error brought up by Rigault et al. in 2016 and found little statistical significance. This result is the most recent measurement using the Cepheid distance ladder and the most precise one up to date.

The Riess et al. (2019) result agrees with the analysis from the Carnegie Hubble Program in 2012, which combines the Spitzer Space Telescope observation with HST Key Project observation [22], which gives a value of $H_0 = 74.3 \pm 2.1$ km s^{-1} Mpc^{-1}. The Carnegie Hubble Program used observations in the mid-infrared range from NASA's Spitzer Space Telescope to find accurate zero-point for Leavitt Law and to reduce other known systematic effects in measuring the Hubble constant.

2.2. Tip of Red Giant Branch Calibration

Following the endeavors of the Hubble Key Project and the Carnegie Hubble Program, the Carnegie-Chicago Hubble Program (CCHP) changes the direction of their efforts and aims to find alternative paths to the distance ladder without using Cepheid calibrations, because there exist certain disadvantages in calibrating distance with Cepheid variables. One inconvenience in the Cepheid distance ladder method is the effects of metallicity, the abundance of elements that are heavier than Hydrogen and Helium present in an astronomical object. The period-luminosity relation of Cepheid variables (Leavitt Law) is affected by its metallicity [23]. The LMC is a low-metallicity galaxy unlike most SNe Ia hosts [24]. As

a result, Cepheid distances in the LMC is difficult to predict and hence the SH0Es project used DEBs to obtain distance to the LMC. Other disadvantages of the Cepheid path include the necessity of additional trigonometric parallax to calibrate the zero point of Leavitt Law and interference from crowding effects. These effects will be discussed in detail in Section 6.2.

The CCHP seeks to establish a different path of distance ladder to calibrate SNe Ia through the Tip of Red Giant Branch (TRGB) [24]. Unlike Cepheid hosts, host galaxies of Red Giant Branch stars are more commonly found throughout the observable universe. Additionally, Red Giant Branch stars are found in stellar halos, so they are less affected by interstellar dust and they aren't influenced by crowding as much as Cepheid variables since the surface brightness in stellar halos tend to be lower.

The first step in the CCHP distance ladder uses trigonometric parallaxes to calibrate the zero point of the period-luminosity relation of RR Lyrae variables. In the second step, we calibrate the absolute brightness of TRGB using the RR Lyrae period-luminosity relation from RR Lyrae variables in the halos six Local Group galaxies as well as the distance to NGC 4258 from megamasers. In the third step, we use the TRGB calibration to find the distance to the host galaxies of of SNe Ia and therefore determine the absolute brightness of those SNe Ia. Then finally, we calibrate a larger population of SNe Ia to measure the Hubble constant.

In 2019, Freedman et al. presented a measurement of H_0 from the CCHP with a result of 69.8 ± 0.8(statistical) $\pm$ 1.7(systematic)km s^{-1} Mpc^{-1} [25]. This measurement lowered the discrepancy between the local H_0 value and the early universe measurement from Planck (2018) to 1.2σ level. This Red Giant Branch calibrated result also agrees with the SH0ES measurement from the Cepheid distance ladder path at 1.7σ level. However, Yuan et al. claim that the Freedman et al. (2019) result overestimated the interstellar extinction towards the Large Magellanic Cloud [26]. Replacing the calibration of the Tip of the Red Giant Branch with the correction by Yuan et al., they find that the H_0 value should be $H_0 = 72.4 \pm 2.0$ km s^{-1} Mpc^{-1} from the Carnegie-Chicago Hubble Program's TRGB path of the distance ladder, pushing the value further from the early universe measurement from Planck (2018). Freedman et al. later refuted this criticism in their 2020 paper [27]. Further details on the Tip of Red Giant Branch calibration method and comparisons between the Cepheid path and the TRGB path to the cosmic distance ladder can be found in Section 6.2.

3. LAMBDA-CDM MEASUREMENTS OF THE HUBBLE CONSTANT

The Standard Model of Cosmology, which is based on the Standard Model of Particle Physics and the theory of General Relativity, explains most of the observational results up till today, including the cosmic microwave background radiation, the large scale structure of galaxy distribution and the expansion of the universe. In the Standard Model of Cosmology, the current universe consists of 5% ordinary matter (baryons, electrons and photons), 68% dark energy, and 27% dark matter [28]. This model is usually referred to as the ΛCDM model, where Λ stands for the cosmological constant which is associated with dark energy and CDM stands for Cold Dark Matter [29].

The standard ΛCDM model is specified by six independent cosmological parameters. We have the freedom, to some extent, to choose this particular set of six parameters [30]. For performing a standard ΛCDM fit on the power spectrum of the cosmic microwave background, a typical set of parameters includes the baryon density $\Omega_b h^2$, the cold dark matter density $\Omega_c h^2$, the Thomson scattering optical depth τ due to reionization, the spectral index of primordial scalar fluctuations n_s, the log power of the amplitude of primordial curvature perturbations $\ln(10^{10} A_s)$, and $100\theta_{MC}$ where θ_{MC} is an approximation to the acoustic scale angle [31, 32]. The acoustic scale angle θ_* is given by $\theta_* \equiv r_*/D_M$, where r_* is the comoving sound horizon at recombination, which tells us the distance that photon-baryon plasma sound waves can travel, and D_M is the comoving angular diameter distance [33]. The angular diameter distance D_A is defined by the ratio of an object's physical size to its angular size as viewed from earth, as illustrated in Figure 5. The comoving angular diameter distance relates to the usual angular diameter distance by $D_M = D_A(1+z)$ where z is the redshift [34]. Figure 6 shows a graph of the relation between angular diameter distance and redshift for different cosmologies.

3.1. Cosmic Microwave Background Experiments

The cosmic microwave background (CMB) is leftover electromagnetic radiation from the Big Bang nearly 14 billion years ago. The scattering process during the recombination period leaves an imprint on the CMB, allowing us to study the global structure of the universe. Spatial temperature fluctuations in the CMB map was first observed by the Cosmic

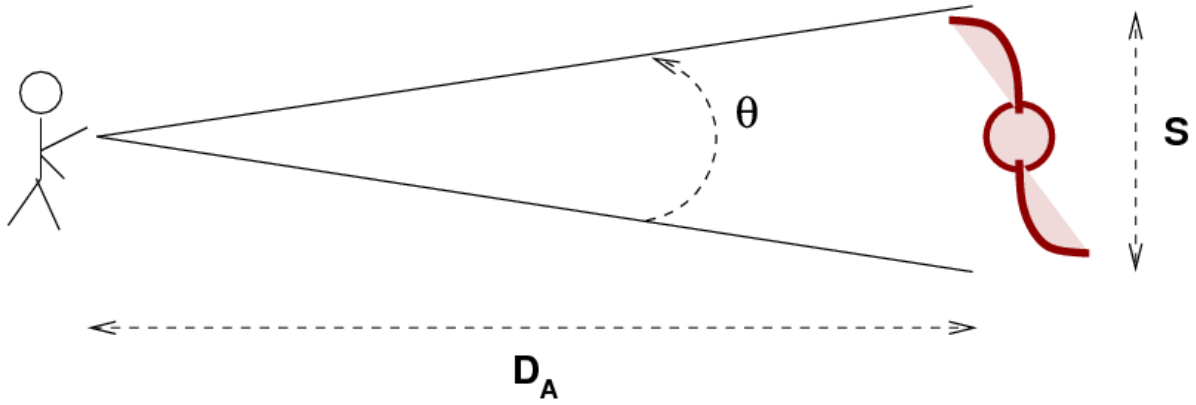

FIG. 5: Diagram illustrating the definition of angular diameter distance. The angular size is denoted θ and the physical size is denoted S [35].

Microwave Background Explorer (COBE) [37]. Later, the Degree Angular Scale Interferometer (DASI) at the South Pole first discovered CMB polarization, left by photons that managed to retain directional information during the scattering process, particularly on the small scales where damping occurs [38, 39]. CMB polarization can be distinguished into the E-mode and B-mode by their properties under a parity transformation on the sphere, analogous to the electric and magnetic fields [40]. Cosmologists extract information from the spatial temperature and polarization fluctuations on the CMB map to learn about the overall structure and early history of the universe.

The fluctuations on the CMB is analyzed through the angular power spectrum. Figure 7 shows an example of the CMB temperature power spectrum observed from the Planck satellite. The vertical axis shows the temperature fluctuation of the CMB detected by Planck. The horizontal axis shows different angular scales of the sky or equivalently, the multipole moment l corresponding to the angular scales. The multipole moment l on the horizontal axis of the power spectrum is associated with angular scales by spherical harmonic analysis. The temperature on the spherical sky expressed in terms of spherical harmonic series is given by

$$T(\theta, \phi) = \sum_{lm} a_{lm} Y_{lm}(\theta, \phi), \tag{3}$$

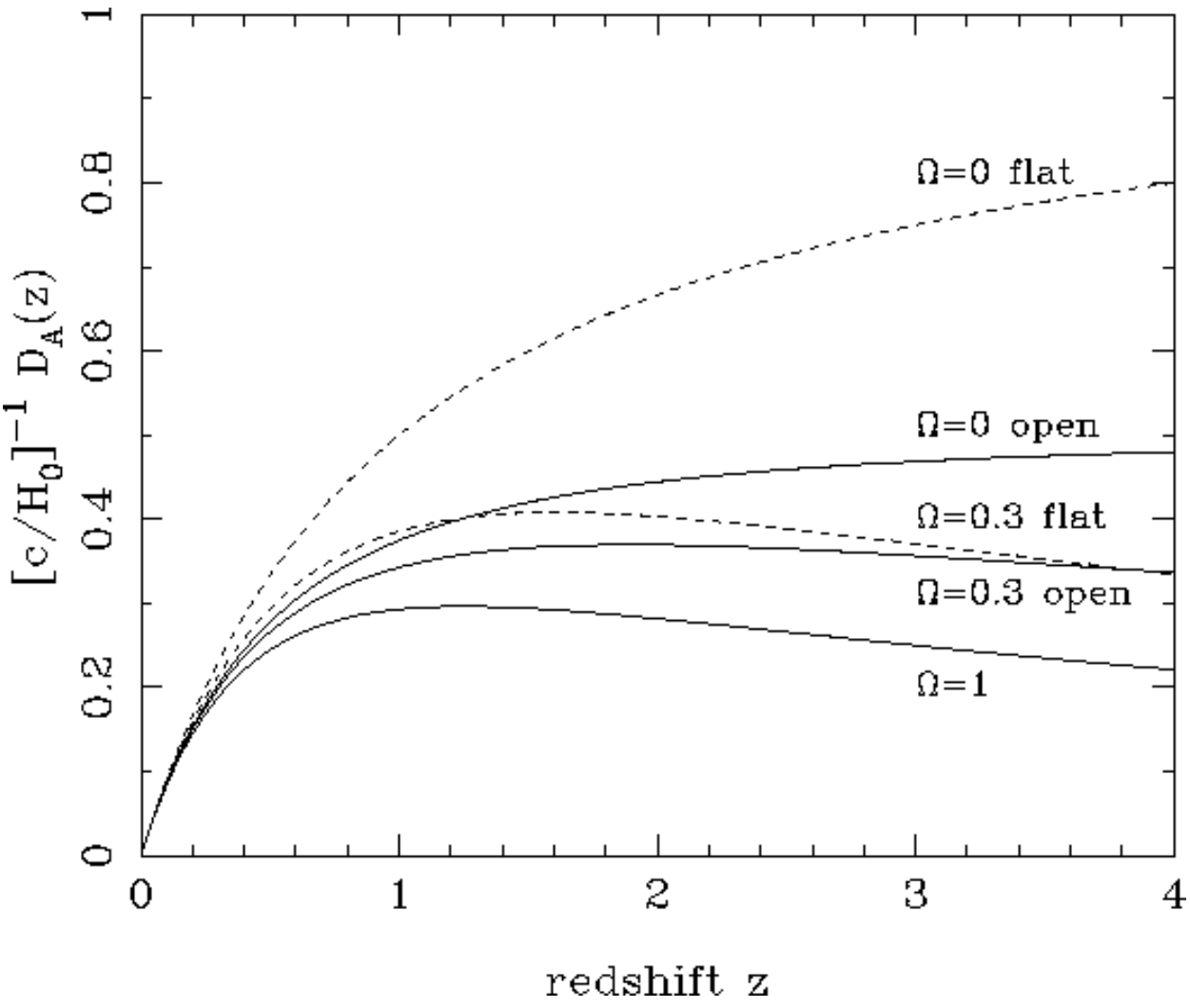

FIG. 6: Plot of angular diameter distance versus redshift for various models of cosmology. Solid lines represent cosmological models with zero vacuum energy. The dashed lines present models in which the universe is flat [36].

where l and m are associated with the number of spatial oscillations on the spherical surface in the θ and ϕ directions. A higher number of spatial oscillations in the θ direction in spherical coordinates is indicated by a higher l, while a higher number of spatial oscillations in the ϕ direction is implied by a higher m. More precisely, there are $(l+1)$ nodes in the θ direction and $(m+1)$ nodes in the ϕ direction.

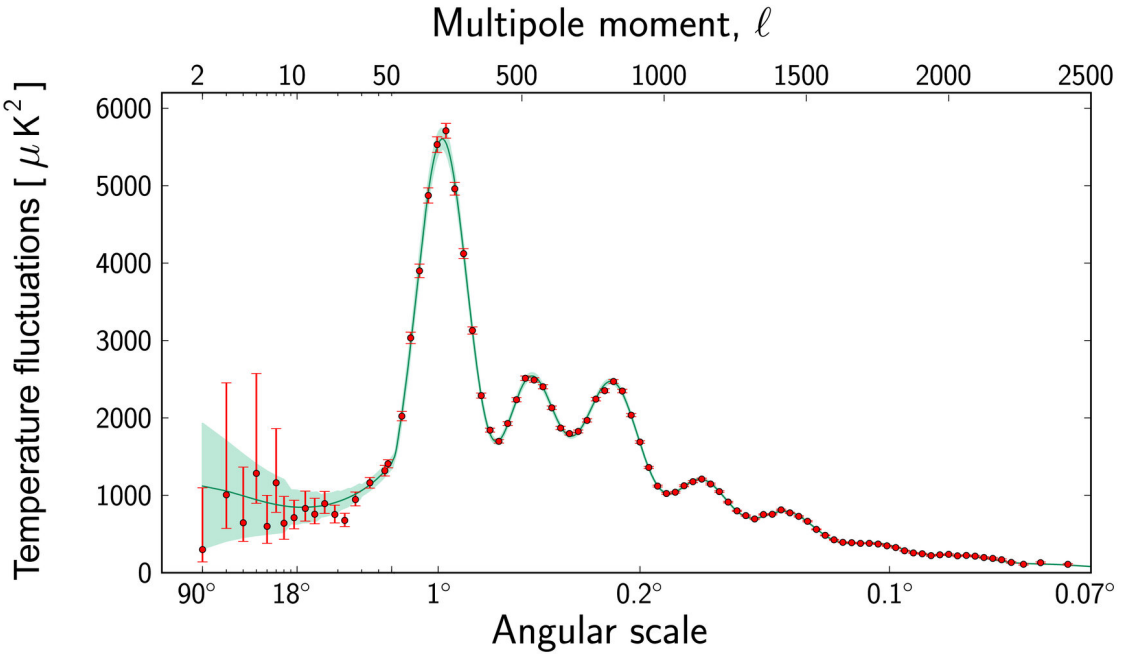

FIG. 7: Temperature power spectrum of the cosmic microwave background from the European Space Agency's Planck satellite [41].

3.1.1. WMAP

The Wilkinson Microwave Anisotropy Probe (WMAP) is a satellite that conducts a full sky map of the cosmic microwave background with angular resolution as fine as 12 arcminutes, ability to detect E mode polarization as well as minimally correlated pixel noise to allow for performance of a full range of statistical tests [42]. Five years after the satellite launched in 2011, Komatsu et al. [43] published the analysis and interpretation of the results from the WMAP five-year data. Fitting the data to a six-parameter ΛCDM model, the WMAP five-year observation alone gives a result of $H_0 = 71.9^{+2.6}_{-2.7}$ km s^{-1} Mpc^{-1}. By combining the WMAP data with Supernovae distance measurements from and Baryon Acoustic Oscillations measurements from galaxy samples [44], they derive a value of $H_0 = 70.5 \pm 1.3$ km s^{-1} Mpc^{-1}. The results slightly vary for different SN compilations, but none of them agree with the latest Riess et al. (2019) [21] distance ladder measurement.

The seven-year data from WMAP fit with a minimal six-parameter flat ΛCDM model produces a value of the Hubble constant $H_0 = 71.0 \pm 2.5$ km s^{-1} Mpc^{-1} [45]. Combining the

WMAP data with Gaussian priors on the BAO distance ratio measurements from the Sloan Digital Sky Survey [46] and the present-day value of Hubble constant from distance ladder measurements [47], Jarosik et al. gives a constraint on the Hubble constant for standard ΛCDM model $H_0 = 70.4^{+1.3}_{-1.4}$ km s^{-1} Mpc^{-1}. The value is still in tension with the distance ladder measurement by Riess et al. (2019) [21].

The six-parameter ΛCDM fit of nine-year WMAP data provides constraint on the value of the Hubble constant $H_0 = 70.0 \pm 2.2$ km s^{-1} Mpc^{-1} [48]. Bennett et al. presents a further analysis combining the full sky CMB data from WMAP with higher resolution CMB measurements from the Atacama Cosmology Telescope (ACT) and the South Pole Telescope (SPT) which only map part of the sky. The combined CMB data together with BAO distance measurements and direct distance ladder measurement of the Hubble constant [15] gives a best fit of $H_0 = 69.32 \pm 0.80$ km s^{-1} Mpc^{-1}. The new observations pushed the result further from the SH0ES measurements and heightened the discrepancy between the early and late universe H_0 values.

3.1.2. Planck

The Planck satellite, affiliated to the European Space Agency (ESA), was launched in May 2009 to study the early universe, in particular the anisotropies in CMB temperature and polarization. Planck is a full sky survey which scans the whole sky twice in one year with angular resolution as fine as 5 arcminutes [49]. When the CMB photons that we observe today travelled across the universe, they were deflected by gravitational potentials from matter density inhomogeneities along the way [50, 51]. This phenomenon is called the weak gravitational lensing on the CMB. A visual representation of the effects of weak lensing on the CMB temperature field is shown in Figure 8. The effects of CMB lensing, although small, need to be accounted for in the analysis of CMB data to produce accurate cosmological parameters. Weak lensing can be observed through the smoothing of the acoustic peaks in the angular power spectrum of the CMB, the generation of B-mode polarization pattern from E-mode polarization and the four-point correlation function, also known as the trispectrum [52]. Planck is the first experiment to measure CMB lensing to a precision significant enough to be used to constrain cosmological parameters [31].

In terms of a minimal six-parameter ΛCDM model, the Planck 2013 data alone gives

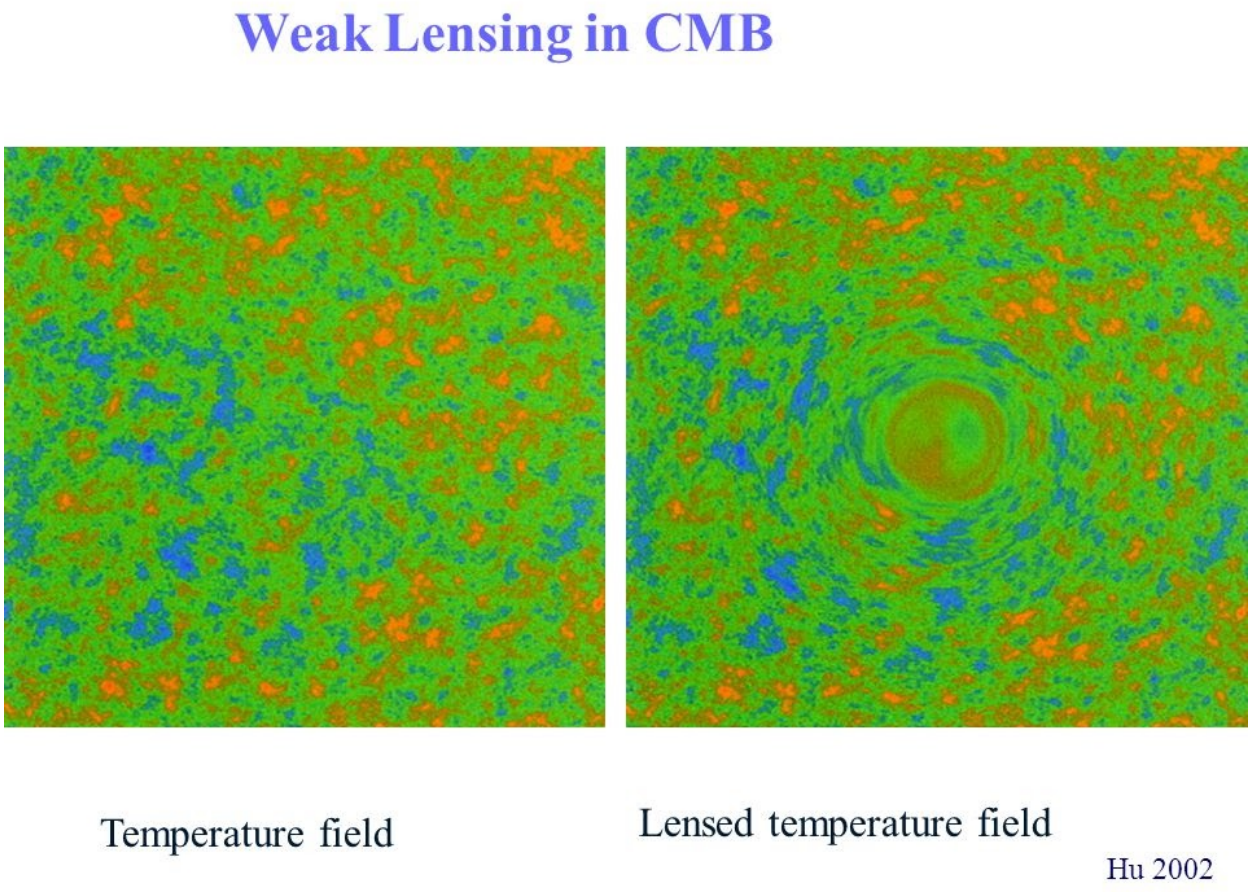

FIG. 8: Comparison of lensed and unlensed maps of the CMB temperature field. [53]

a 68% confidence interval of $H_0 = 67.4 \pm 1.4$ km s^{-1} Mpc^{-1} [33]. Note that because the CMB likelihood is not well approximated at low multiples ($l \lesssim 50$), so low-l likelihood is analyzed separately [54]. Planck 2013 analysis takes advantage of low-l polarization data from WMAP and high-l polarization from higher resolution surveys, namely the ACT ($l \gtrsim 1000$) and the SPT ($l > 2000$) [55]. Including the WMAP low-l polarization tightens the constraint to $H_0 = 67.3 \pm 1.2$ km s^{-1} Mpc^{-1}. Combining Planck, WMAP polarization, high-l spectra from ACT and SPT as well as BAO measurements further tightens the constraint to $H_0 = 67.80 \pm 0.77$ km s^{-1} Mpc^{-1} to 68% limits [33]. The Planck 2013 result of the Hubble constant is in agreement with the WMAP nine-year result within 1σ, although lower than the Riess et al. (2019) result by almost 5σ.

The Planck 2015 result [56] is consistent with that from the previous data release, with a value of $H_0 = 67.27 \pm 0.66$ km s^{-1} Mpc^{-1} from Planck alone. Instead of WMAP polar-

ization, Planck 2015 analysis uses its low-l polarization reconstruction ($l \leq 29$) from Planck High Frequency Instrument (HFI) [57]. By including BAO measurements, the constraint is tightened to $H_0 = 67.90 \pm 0.55$ km s^{-1} Mpc^{-1}. By including the CMB lensing spectrum, the analysis produces slightly tighter confidence interval $H_0 = 67.51 \pm 0.64$ km s^{-1} Mpc^{-1}. Further including data from BAO, Joint Light-curve Analysis of SNe and priors on direct Hubble constant measurements from distance ladder, the constraint tightens to $H_0 = 67.74 \pm 0.46$ km s^{-1} Mpc^{-1} [56]. Similar to the Planck 2013 analysis, a significant discrepancy is evident between the Planck and the SH0ES measurements.

Similar to the 2015 analysis, the Planck 2018 data release [31] gives $H_0 = 67.27 \pm 0.60$ km s^{-1} Mpc^{-1} at 68% confidence interval using Planck temperature and polarization, with additional low-l EE likelihood from Planck HFI. Note that EE denotes an auto power spectrum for E-mode polarization, TT an auto power spectrum for temperature and TE a cross-spectrum between temperature and E-mode polarization. Including the lensing power spectrum produces result $H_0 = 67.35 \pm 0.54$ km s^{-1} Mpc^{-1}. Combining Planck temperature and polarization power spectra, CMB lensing reconstruction and BAO measurements gives a tight constraint $H_0 = 67.66 \pm 0.42$ km s^{-1} Mpc^{-1} which is in very well agreement with the result from the previous Planck data release [31, 56], and naturally still in tension with the SH0ES measurement [21].

3.1.3. Other CMB Observations

The Atacama Cosmology Telescope (ACT), as mentioned previously, is a ground based telescope located in the Atacama desert in Chile designed to make high resolution CMB maps that covers over half of the sky. The telescope contains a polarization sensitive component ACTPol, which consists of three detector arrays that operate at different frequencies. The angular resolution of the ACT reaches as fine as one arcminute [58]. A standard ΛCDM fit of the CMB likelihood from ACT data produces a value of $H_0 = 67.9 \pm 1.5$ km s^{-1} Mpc^{-1} [59]. This result is in well agreement with that from the Planck full-sky map.

The South Pole Telescope (SPT), as mentioned previously in the Planck discussion, is a 10-meter diameter telescope based in Antarctica at the Amundsen-Scott South Pole station commissioned for high resolution CMB observations. The South Pole Telescope Sunyaev-Zel'dovich (SPT-SZ) survey covers around 2500deg^2 of the sky with angular reso-

lution as fine as one arcminute [60]. Using the SPT-SZ data alone with a Gaussian prior of the optical depth to reionization τ from WMAP 7-year observational results, Story et al. (2013) derives the Hubble constant from a standard 6-parameter ΛCDM best fit $H_0 = 75.0 \pm 3.5$ km s^{-1} Mpc^{-1}. Combining SPT data with the full WMAP 7-year likelihood and priors of direct H_0 measurement from Riess et al. (2011) tightens the constraint to $H_0 = 73.0 \pm 1.5$ km s^{-1} Mpc^{-1} [32]. Both results are in agreement with the SH0ES distance ladder measurements. However, combining SPT and WMAP data with BAO distance measurements at different redshifts from the WiggleZ survey, the SDSS-II survey and the BOSS survey introduces tension with the Cepheid distance ladder measurements, with a value of $H_0 = 69.11 \pm 0.85$ km s^{-1} Mpc^{-1}. Adding a Gaussian prior for direct H_0 measurement slightly tightens the constraint to $H_0 = 69.62 \pm 0.79$ km s^{-1} Mpc^{-1}, while the tension with the SH0ES result remains [32].

The polarization sensitive detector SPTpol was equipped on the SPT with arcminute resolution at 150GHz and collected data from 2012 through 2016 [60]. Henning et al. (2018) analyzed the EE auto-power spectrum and the TE cross-power spectrum from SPTpol observations and find the constraint on the Hubble constant to be $H_0 = 67.49 \pm 3.99$ km s^{-1} Mpc^{-1} for a standard ΛCDM fit when using the low-l data set ($50 < l \leq 1000$). This result is consistent with the constraint from the Planck TT power spectrum. However, the 68% marginalized constraint from the high-l SPTpol data set ($1000 < l \leq 8000$) $H_0 = 73.49 \pm 3.73$ km s^{-1} Mpc^{-1} is at an almost 2σ discrepancy with that from the low-l data set. The constraint from the full multipole range ($50 < l \leq 8000$) data gives a value of $H_0 = 71.29 \pm 2.12$ km s^{-1} Mpc^{-1}, which is still in over 1σ tension with the result from SPTpol low-l data as well as that from Planck TT spectrum [61].

More recently, Bianchini et al. (2020) analyzed the CMB lensing measurement from the SPTpol survey. Combination of the likelihood from SPTpol lensing potential power spectrum with BAO measurements gives constraint $H_0 = 72.0^{+2.1}_{-2.5}$ km s^{-1} Mpc^{-1} for standard ΛCDM, which is in around 2σ tension with the best fit from Planck lensing combined with BAO observations [62]. More details about the inconsistencies between difference CMB measurements will be discussed in Section 6.3.

4. BARYON ACOUSTIC OSCILLATIONS MEASUREMENTS

Baryon Acoustic Oscillations (BAO) are perturbations of baryonic matter in the early universe produced by radiation pressure in the relativistic primordial plasma. The coupling between photons and baryons imprints these fluctuations onto the power spectrum of matter perturbations. At the recombination epoch, the decoupling of matter and radiation leaves the acoustic peaks onto the CMB power spectrum [46, 63]. An illustrative example of acoustic peaks in the CMB power spectrum is shown in Figure 9. The sound horizon, conventionally denoted r_s, is the radius to which the sound waves in the baryon-photon plasma can travel by the time of recombination [64]. The sound horizon is easy to estimate from underlying physics depending on sound speed and expansion rate in the early universe [65]. Therefore, the physical scale of the sound horizon engraved in the CMB anisotropies at recombination provides a "standard ruler" to study the geometry of the universe and to constrain cosmological parameters [44]. The length of this standard ruler can also be measured from the power spectrum of large-scale galaxy redshift surveys [66]. The agreement between the galaxy survey measurements and CMB measurements would greatly increase the credibility of our cosmological models.

To make a good measurement of the Hubble constant, we may combine BAO and SNe into an "inverse distance ladder". Contrary to the traditional Cepheid distance ladder, the inverse distance ladder uses the distance scale from BAO in galaxy distributions, often combined with Gaussian priors of certain parameters from CMB, to calibrate the absolute magnitude of SNe, instead of using calibration from Cepheid period-luminosity relations. Rather than beginning at low redshift measurements and working its way further, the inverse distance ladder is anchored at intermediate redshift galaxy surveys and transfers absolute distance measurements of the BAO scale to low redshift SNe relative distance measurements [68]. The slope of the distance-redshift relation converges to H_0 at very low redshift, allowing us to easily obtain the value of the Hubble constant. This method is independent from assumptions of dark energy behavior and curvature at higher redshifts.

Data from the Sloan Digital Sky Survey (SDSS) [69] and the 2-degree Field Galaxy Redshift Survey (2dFGRS) [70] offer power spectra for observing BAO at different redshifts. Using the constraints on the physical baryon density $\Omega_b h^2$ and the physical cold dark matter density $\Omega_c h^2$ from the WMAP five-year data [43] as Gaussian priors, Percival et al. (2010)

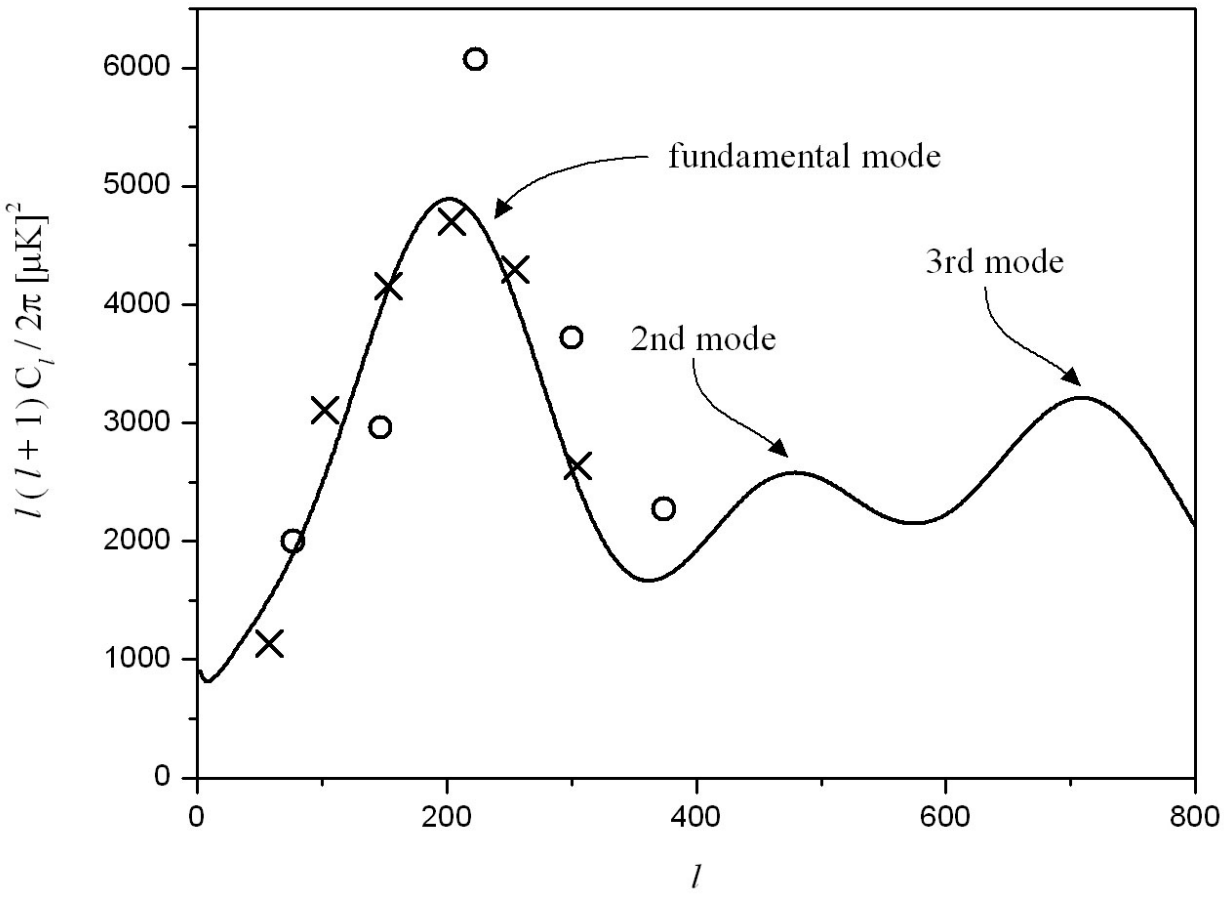

FIG. 9: A schematic example of acoustic peaks in the CMB power spectrum. The solid curve is the theoretical power spectrum and the crosses and circles are representative data point. [67]

combine BAO distance measurements from the SDSS and 2dFGRS with relative distance measurements from the Union Supernova sample to find a value for the Hubble constant $H_0 = 68.2 \pm 2.2$ km s^{-1} Mpc^{-1} [46] for a flat ΛCDM fit. This constraint does not include the angular acoustic scale from the CMB and is therefore insensitive to dark energy models at redshifts higher than the galaxy samples. For the same flat ΛCMD model, the combination the BAO measurements and the full 5-year WMAP likelihood, including acoustic scales on the CMB, gives a value of $H_0 = 70.1 \pm 1.5$ km s^{-1} Mpc^{-1} [46]. This constraint is now sensitive to dark energy behavior at high redshifts.

Although the BAO peaks serves as a useful anchor for calibrating cosmological scales, it experiences a damping that reduces its accuracy as a standard ruler. Tidal gravitational forces generates bulk motions that result in the damping of the acoustic oscillations [71]. Eisenstein et al. introduced a technique to reconstruct the baryon acoustic feature by using

the density field to estimate the displacement cause by the bulk motions [72]. Kazin et al. (2014) used this baryon feature reconstruction method to obtain distance measurements from the WiggleZ Dark Energy Survey, a galaxy redshift survey which produces large scale structure power spectra used for the detection of baryonic acoustic oscillations [73]. By combining the reconstructed BAO measurements from WiggleZ and 6-degree Field Galaxy Redshift Survey (6dFGRS) with the Planck temperature power spectrum and the WMAP five-year polarization detection, the standard ΛCDM fit gives a constraint on the Hubble constant $H_0 = 67.15 \pm 0.98$ km s^{-1} Mpc^{-1} [71]. This value deviates for 2.6σ from the SH0ES measurement [15].

In 2015, Aubourg et el. used the inverse distance ladder to obtain a measurement of $H_0 = 67.3 \pm 1.1$ km s^{-1} Mpc^{-1} [68]. They made use of the measurements from SDSS-III Baryon Oscillation Spectroscopic Survey (BOSS), a survey of large scale structure to measure the baryonic acoustic oscillations in the clustering of matter [74]. They constructed the inverse distance ladder using the BAO measurements from BOSS, analysis of Type Ia SNe as well as the physical scale of the sound horizon calibrated by the CMB data from Planck and WMAP. The Hubble constant yielded from this analysis is in over 5σ tension with the SH0ES measurement [21].

5. STRONG GRAVITATIONAL LENSING MEASUREMENTS

Even before the multi-imaging due to strong gravitational lensing was first observed in 1979 by Walsh et al. [75], theorists had already introduced the time delay method to constrain cosmological constants by gravitational lensing [76]. By basic laws of general relativity, when light travels nearby a massive galaxy, it gets deflected towards the large mass, which we call the foreground lens galaxy. The galaxy being observed through the gravitational lens is called the background source galaxy. When the line of sight of the observer to the foreground lens galaxy is close to the background source galaxy without directly going through it, the source galaxy is multi-imaged since the light follows different paths around the lens galaxy [77]. As shown in Figure 10, two paths of the light rays from the source galaxy reach the observer at different times due to the difference in length, resulting in a geometric time delay between the two images of the source galaxy through the gravitational lens. Taking into account of the time dilation near a massive object, we find

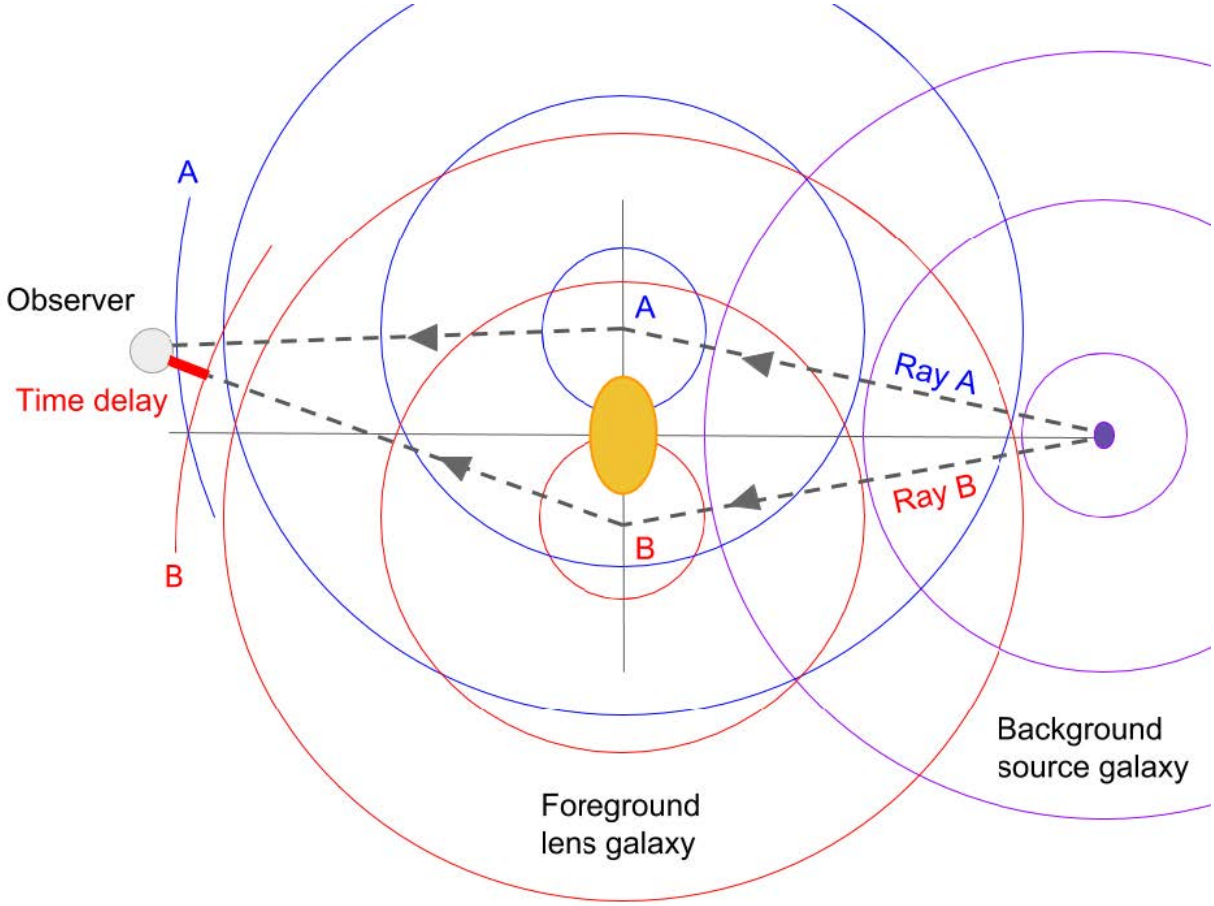

FIG. 10: Illustration of the geometric aspect of time delay [77].

the total contribution to the lens time delay, which is measurable when the luminosity of the source object varies in time. We find the time-delay distance from the measurable delay time and the mass distribution of the lensing foreground [78]. The time-delay distance as well as the red-shifts of the foreground and background objects in turn allows us to calculate the Hubble constant [76]. The background sources used for the gravitational time-delay method are usually object and events with variable luminosity such as supernovae and active galactic nuclei.

The H0 Lenses in COSMOGRAIL's Wellspring (H0LiCOW) project aims to measure H_0 to 3.5% precision using the time-delay method for five strong gravitational lensing systems [78]. Note that the time-delay distance is a combination of the angular diameter distances to the deflector and to the source object as well as the angular diameter distance between the lens and the source. Using the velocity dispersion and mass profile of the lens galaxy as well

as lensed images of the background source, we can measure the angular diameter distance to the lens galaxy [79, 80]. Jee et al. (2016) finds that including the angular diameter distance to the lens in addition to the time-delay distance improves the constraints on cosmological parameters from strong lensing time-delay systems [81].

The H0LiCOW program therefore needs four major components to accurately and precisely measure the Hubble constant from the five lensing systems. The first component is time delays, which are obtained from COSMOGRAIL (COSmological MOnitoring of GRAvItational Lenses) and the Very Large Array. The second component is high resolution images of the lens systems from the Hubble Space Telescope. The third component is the characterization of the lens environment from wide-field imaging and spectroscopy. The final ingredient is the stellar velocity dispersion of the lens galaxy to model the mass distribution and to measure the angular diameter distance to the lens [78].

In 2017, the H0LiCOW project gives a result of $H_0 = 71.9^{+2.4}_{-3.0}$ km s^{-1} Mpc^{-1} for a flat ΛCDM cosmology with no prior assumption on the matter density parameter Ω_m from the Time Delays Strong Lensing Probe alone [82], independent from the traditional distance ladder and the CMB experiments. When combined with the Planck 2015 results and assuming $\Omega_m = 0.32$ [56], H0LiCOW analysis yields a value of $H_0 = 72.8 \pm 2.4$ km s^{-1} Mpc^{-1} [82]. Both of these results are in agreement with distance ladder values by Riess et al. in recent years to 1σ [19, 21, 83]. They are also in agreement with the re-estimation of the Freedman et al. (2016) [25] TRGB result from the Carnegie-Chicago Hubble Program by Yuan et al. [26], although in tension with the original CCHP results and the Planck results. Combining the time delay strong lensing method with Planck data and using a non-flat ΛCDM cosmology, the H0LiCOW measurements gives the Hubble constant $H_0 = 69.2^{+1.4}_{-2.2}$ km s^{-1} Mpc^{-1} and the curvature $\Omega_k = 0.003^{+0.004}_{-0.006}$, which agree with the flat universe model.

In 2019, Wong et al. updated the latest results from the H0LiCOW projects with a 2.4% percent uncertainty H_0 measurement [84]. Using the time delays of six gravitationally lensed quasars, they obtain a value of $H_0 = 73.3^{+1.7}_{-1.8}$ km s^{-1} Mpc^{-1} in a flat ΛCDM cosmology, which in 3.1σ discrepancy with the Planck measurement. Allowing for curvature gives $H_0 = 74.4^{+2.1}_{-2.3}$ km s^{-1} Mpc^{-1} and $\Omega_k = 0.26^{+0.17}_{-0.25}$. The result of the non-flat ΛCDM analysis is distinct from that of the flat ΛCDM model, but allowing for curvature failed to resolve the tension with the CMB measurements. Both of these results are in agreement with the latest Cepheid distance ladder measurement by Riess et al. (2019) [21]. Combining the time

delay measurements with the distance ladder results from the SH0ES collaboration further pushes the tension with the Planck results further to 5.3σ [84].

6. DISCREPANCY BETWEEN MEASUREMENTS AND POTENTIAL SYSTEMATIC ERRORS

6.1. Summary of Different Results

Table I shows the values of the Hubble constant measured from the latest observations of major experiments using different methods. The values from the CMB experiments, WMAP, Planck, ACT and SPT, are mostly in agreement at least in the low-l range, so here we choose the latest Planck value as a representative of CMB measurements to compare with measurements from other methods of observation. The major tension between the different values is the 4.4σ discrepancy between the SH0ES local measurement and the CMB measurement from Planck. The CMB measurement is well supported by the measurement from BAO inverse distance ladder. However, the strong gravitational lensing measurements from the H0LiCOW project, independent from the usual distance ladder approach, offer more evidence for the higher H_0 value as observed by the SH0ES project.

The latest analysis from the Carnegie-Chicago Hubble Program with the Tip of Red Giant Branch distance ladder, most interestingly, shows no statistically significant discrepancy between the TRGB measurement and the CMB measurements of the Hubble constant [85]. The H_0 value from the latest TRGB calibration, however, deviates from the Cepheid measurements for almost 2σ. Understanding the discrepancy between the results from those two different calibrations of the distance ladder approach is most promising to shed light on the possibilities of unknown systematic errors in the Cepheid calibrations.

SH0ES (Cepheid)	CCHP (Tip of Red Giant Branch)	Planck	Inverse Distance Ladder	H0LiCOW
74.03 ± 1.62	$69.8 \pm 0.6(\text{stat}) \pm 1.6(\text{sys})$	67.27 ± 0.60	67.3 ± 1.1	$73.3^{+1.7}_{-1.8}$

TABLE I: Values of H_0 from different experiments in units of km s^{-1} Mpc^{-1}.

6.2. Comparison of Cepheids and TRGB as Distance Indicators

Freedman et al. (2021) [85] gives a comprehensive comparison of distance measurements from TRGB and Cepheids with respect to their reliability as standard candles, the effects on crowding/blending on photometry for each method, the effects of dust and metallicity, as well as the consistency of the calibrations for their respective zero point from different observations.

As explained previously in the introduction, Cepheid variable stars follow a period-luminosity relation which allows astronomers to use them as standard candles for distance calibrations. However, their luminosity does vary and we are fully dependent on a well-defined period-luminosity relation when using Cepheids as part of the distance ladder. Although applications of Leavitt Law is highly precise and well understood, Cepheids are still technically "standardizable candles" instead of actual standard candles. The same situation applies to SNe, and we have seen the standardization of SNe light curves in Figure 4.

Tip of Red Giant Branch is the upper limit of the luminosity of stars with a degenerate helium core in the red giant branch of stellar evolution, which can be easily observed as a feature in the Hertzsprung–Russell diagram, also known as the color-magnitude diagram. An example of what a Hertzsprung-Russel diagram looks like is shown in Figure 11. When the helium core reaches sufficient temperature, nuclear fusion begins and the luminosity of the red giant branch star rapidly decreases. This process is called the helium flash, and its occurrence is highly dependent on the temperature in the stellar core [86]. The helium flash always happens at around the same core temperature and therefore the same luminosity, making TRGB actual standard candles.

In crowded regions in a galaxy, the flux from background stellar crowd overlaps with the object being observed, rendering the target object indistinguishable from the background. This phenomenon is called "crowding" in astronomical photometry [88]. A similar term is "blending", which describes two or more stars along a line of sight overlapping and causing them to be unresolved in the imaging process [89, 90].

The TRGB calibration method is mainly applied in the halos of galaxies rather than in their disks for maximum precision and accuracy [91]. The brightness in the halos of a galaxy is relatively low compared to the brightness of the Helium flash, so the effects of crowding and blending on the TRGB method is minimal. Cepheid variables, however, are usually

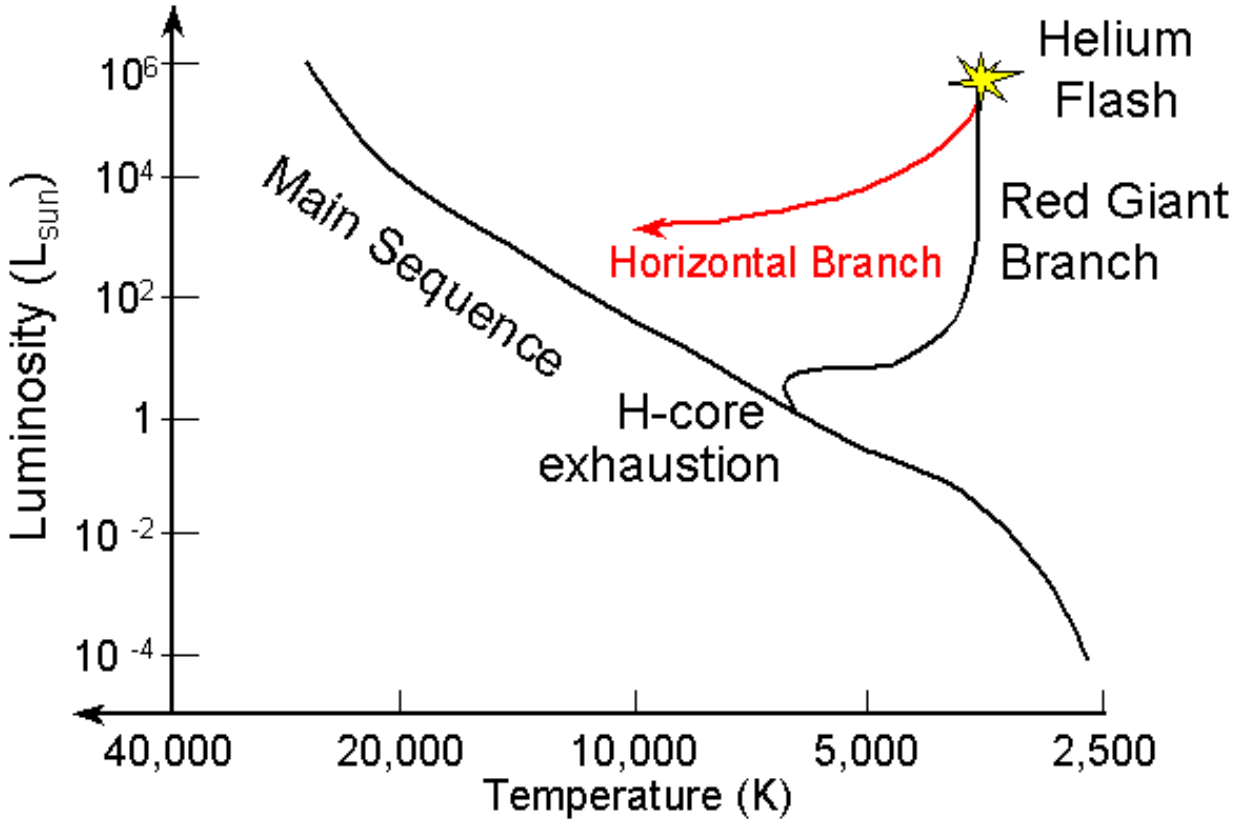

FIG. 11: A sketch of a typical Hertzsprung-Russell diagram [87]. The first few stages of the evolution of low-mass stars, namely the Main Sequence Phase, the core Hydrogen exhaustion and the Red Giant Branch, are labeled on the diagram. The highest point on the Red Giant Branch, where Helium Flash occurs, is the Tip of Red Giant Branch.

found in star-forming disks of galaxies where the luminosity of background objects tend to be relatively high. Crowding/blending thus becomes a problem for the Cepheid variable method, especially for Cepheids that are further away due to decreased angular resolution. The resolution also worsens for aperture telescopes at higher wavelengths and aggravates the crowding/blending problem. For the Cepheid calibration method, lower wavelengths are preferred to avoid the crowding/blending effect.

Cepheid variables were formed relatively recently, and they are inevitably located near the dust and gas from which they birthed. Fortunately, the effects of dust on Cepheid variables are well understood and easily compensated for [92]. Specifically, the effects of dust on Cepheid variables decrease with as wavelength increases. The effects of metallicity on the Cepheid period-luminosity relation is still being heavily debated, but it has been suggested

that the effects are smaller at higher wavelengths. Therefore, if we want to accurately use the Cepheid method for distance ladder calibrations, there is a trade-off between minimizing the effects of dust and metallicity and increasing resolution to avoid crowding/blending as the optimal wavelengths are different for lowering these effects.

The effects of dust on the TRGB leads to a systematic uncertainty in the measurement of H_0 when only one individual galaxy is used as the anchor. An example of such analysis on the systematic uncertainty due to the effects of dust on the TRGB method can be found in Ref. [93], where Jang et al. discuss the TRGB method for Hubble constant measurement applied in the halo of NGC1365. Although a systematic uncertainty is present for an individual anchor, when multiple anchors are used for H_0 measurement, the effects of dust only contribute to the overall statistical uncertainty, rather than a systematic error [85].

The relationship between the color and the metallicity of stars on the Red Giant Branch has been observed for decades [94, 95] and is commonly used to determine the metallicity of Red Giant Branch stars [96]. Theoretical simulations of TRGB behaviors [97], including the relationship between wavelengths, luminosity and metallicity, have been confirmed by empirical observations [27]. The effects of metallicity on the TRGB method is clearly understood both theoretically and empirically.

The direct geometric calibrations of TRGB zero point from different galaxies yield values of the Hubble constant that are consistent within 1%. Meanwhile, the direct geometric calibrations of the zero point of the Cepheid Leavitt Law from different calibration methods result in H_0 values that vary for up to around 3%.

Overall, the TRGB path of the distance ladder appears to be more reliable than the Cepheid method, especially in terms of the effects of crowding, dust and metallicity. Yuan et al. (2019) reanalyzed the 2019 CCHP results and concluded that the calibration of TRGB in the Large Magellanic Cloud by Freedman et al. (2019) was inaccurate due to their overestimate of distinction in the LMC. However, Freedman et al. rebuked the critique from Yuan et al. (2019) in their 2020 paper by pointing out the misunderstandings and erroneous assumptions in the reanalysis by Yuan et al. [27].

6.3. Inconsistencies within the CMB Measurements

As mentioned previously in Section 3.1, there exists an around 2σ tension between the best fit value for the Hubble constant from the SPTpol survey and the value from the Planck observations [61]. Analysis by Aylor et al. (2017) indicates that the Planck and SPT data are highly consistent when restricted to the same range of l-modes ($650 \leq l \leq 2000$) and the same patch of the sky, which means picking the part of the full sky Planck survey which overlaps with the patch of the sky covered by the SPT survey. The discrepancy between the Planck best fit values and the SPT best fit values comes from both the fact that the Planck survey covers a larger portion of the sky and the fact that the SPT survey includes data with higher multipoles ($l > 2000$). The high-l data observed by the SPT shifts the baryon matter density as well as the total matter density to a lower value, and thus driving H_0 to a higher value than the low-l measurements [98].

In addition to the discrepancy between the Planck and SPT data, internal inconsistency appears within the Planck observations as well. Addison et al. (2016) examined the Planck 2015 data and found tension between the ΛCDM cosmological parameters derived from lower-l ($l < 1000$) and higher-l ($l \geq 1000$) data. The high multipole data shift the value of the Hubble constant down to $H_0 = 64.1 \pm 1.7$ km s^{-1} Mpc^{-1}, which is 2σ away from the low-l measurement $H_0 = 69.7 \pm 1.7$ km s^{-1} Mpc^{-1} [99]. Note that high-l Planck data and high-l SPT data drives the H_0 value from the low-l best fit in opposite directions. This result suggests that there may be unknown systematic effects happening at small angular scales for Planck, SPT and other CMB experiments. For this reason, we will exclude these two high-l measurements from SPT and Planck 2015 in the following discussion when comparing to the measurements from other observational methods.

Planck 2018 data also shows a split of parameter values between the $l \leq 800$ data and the $l > 800$ data. This discrepancy is found to be due to significant mismatch between the data for very large angular scales, reaching as low as $l < 30$, and the rest of the data [31]. The details about this "low-l deficit" can be found in the Planck 2017 intermediate results [100]. Fortunately, the analysis in the Planck 2017 intermediate results concluded that the parameter shifts from this discrepancy is not significant enough to require searching for systematic errors that have not been accounted for.

7. CONCLUSION

From our comparisons among various attempts to measure the Hubble constant, the most reliable result in the distance ladder regime is the latest measurement from CCHP using the TRGB method, with a value of 69.8 ± 0.6(statistical) $\pm$ 1.6(systematic)km s^{-1} Mpc^{-1} [85]. The most credible result among the CMB measurements is the latest value from the Planck experiment, $H_0 = 67.27 \pm 0.60$ km s^{-1} Mpc^{-1} [31]. These two values are in agreement up to 1σ, which strongly suggests that the existence of Hubble tension is caused by unknown systematic effects in the observations rather than new physics. Meanwhile, current understanding and analysis for the systematic error of the Cepheid experiments failed to explain the discrepancy between the Cepheid and TRGB values and the current value from the SH0ES project is supported by strong gravitational lensing observations from H0LiCOW. Fortunately, with the upcoming launch of new experiments and improvements on existing observations, the resolution of Hubble tension is promising in the near future.

[1] W. L. Freedman, *Cosmology at at crossroads: Tension with the hubble constant* (2017), 1706.02739.

[2] N. A. Bahcall, Proceedings of the National Academy of Sciences **112**, 3173 (2015), ISSN 0027-8424, https://www.pnas.org/content/112/11/3173.full.pdf, URL https://www.pnas.org/content/112/11/3173.

[3] S. Howard, Journal of the Washington Academy of Sciences **97**, 47–64 (2011), URL https://www.jstor.org/stable/24536521.

[4] E. Hubble, Proceedings of the National Academy of Sciences **15**, 168 (1929), ISSN 0027-8424, https://www.pnas.org/content/15/3/168.full.pdf, URL https://www.pnas.org/content/15/3/168.

[5] (2011), URL https://www.uwa.edu.au/science/-/media/Faculties/Science/Docs/Explanation-of-the-cosmic-distance-ladder.pdf.

[6] R. W. Pogge, *Lecture 5: Distances of the stars*, URL http://www.astronomy.ohio-state.edu/~pogge/Ast162/Unit1/distances.html.

[7] E. L. Wright, URL http://www.astro.ucla.edu/~wright/distance.htm.

[8] G. F. Benedict, B. E. McArthur, M. W. Feast, T. G. Barnes, T. E. Harrison, R. J. Patterson, J. W. Menzies, J. L. Bean, and W. L. Freedman, Astron. J. **133**, 1810 (2007), [Erratum: Astron.J. 133, 2980 (2007)], astro-ph/0612465.

[9] H. S. Leavitt and E. C. Pickering, Harvard College Observatory Circular **173**, 1 (1912).

[10] M. Hamuy, J. Maza, M. M. Phillips, N. B. Suntzeff, M. Wischnjewsky, R. C. Smith, R. Antezana, L. A. Wells, L. E. Gonzalez, P. Gigoux, et al., **106**, 2392 (1993).

[11] M. M. Phillips, **413**, L105 (1993).

[12] A. Sandage, The Astrophysical Journal **402**, 3 (1993).

[13] G. D. Vaucouleurs and W. L. Peters, The Astrophysical Journal **248**, 395 (1981).

[14] W. L. Freedman, B. F. Madore, B. K. Gibson, L. Ferrarese, D. D. Kelson, S. Sakai, J. R. Mould, R. C. Kennicutt, Jr., H. C. Ford, J. A. Graham, et al., The Astrophysical Journal **553**, 47–72 (2001), ISSN 1538-4357, URL http://dx.doi.org/10.1086/320638.

[15] A. G. Riess, L. Macri, S. Casertano, H. Lampeitl, H. C. Ferguson, A. V. Filippenko, S. W. Jha, W. Li, and R. Chornock, The Astrophysical Journal **730**, 119 (2011), ISSN 1538-4357, URL http://dx.doi.org/10.1088/0004-637X/730/2/119.

[16] I. Ribas, E. L. Fitzpatrick, F. P. Maloney, E. F. Guinan, and A. Udalski, The Astrophysical Journal **574**, 771–782 (2002), ISSN 1538-4357, URL http://dx.doi.org/10.1086/341003.

[17] M. Hicken, P. Challis, S. Jha, R. P. Kirshner, T. Matheson, M. Modjaz, A. Rest, W. M. Wood-Vasey, G. Bakos, E. J. Barton, et al., The Astrophysical Journal **700**, 331 (2009), URL https://doi.org/10.1088/0004-637x/700/1/331.

[18] M. Rigault, G. Aldering, M. Kowalski, Y. Copin, P. Antilogus, C. Aragon, S. Bailey, C. Baltay, D. Baugh, S. Bongard, et al., The Astrophysical Journal **802**, 20 (2015), ISSN 1538-4357, URL http://dx.doi.org/10.1088/0004-637X/802/1/20.

[19] A. G. Riess, S. Casertano, W. Yuan, L. Macri, B. Bucciarelli, M. G. Lattanzi, J. W. MacKenty, J. B. Bowers, W. Zheng, A. V. Filippenko, et al., The Astrophysical Journal **861**, 126 (2018), ISSN 1538-4357, URL http://dx.doi.org/10.3847/1538-4357/aac82e.

[20] A. G. A. Brown, A. Vallenari, T. Prusti, J. H. J. de Bruijne, C. Babusiaux, C. A. L. Bailer-Jones, M. Biermann, D. W. Evans, L. Eyer, and et al., Astronomy Astrophysics **616**, A1 (2018), ISSN 1432-0746, URL http://dx.doi.org/10.1051/0004-6361/201833051.

[21] A. G. Riess, S. Casertano, W. Yuan, L. M. Macri, and D. Scolnic, The Astrophysical Journal **876**, 85 (2019), ISSN 1538-4357, URL http://dx.doi.org/10.3847/1538-4357/ab1422.

[22] W. L. Freedman, B. F. Madore, V. Scowcroft, C. Burns, A. Monson, S. E. Persson, M. Seibert, and J. Rigby, The Astrophysical Journal **758**, 24 (2012), ISSN 1538-4357, URL http://dx.doi.org/10.1088/0004-637X/758/1/24.

[23] W. Gieren, J. Storm, P. Konorski, M. Górski, B. Pilecki, I. Thompson, G. Pietrzyński, D. Graczyk, T. G. Barnes, P. Fouqué, et al., Astronomy Astrophysics **620**, A99 (2018), ISSN 1432-0746, URL http://dx.doi.org/10.1051/0004-6361/201833263.

[24] R. L. Beaton, W. L. Freedman, B. F. Madore, G. Bono, E. K. Carlson, G. Clementini, M. J. Durbin, A. Garofalo, D. Hatt, I. S. Jang, et al., The Astrophysical Journal **832**, 210 (2016), ISSN 1538-4357, URL http://dx.doi.org/10.3847/0004-637X/832/2/210.

[25] W. L. Freedman, B. F. Madore, D. Hatt, T. J. Hoyt, I. S. Jang, R. L. Beaton, C. R. Burns, M. G. Lee, A. J. Monson, J. R. Neeley, et al., The Astrophysical Journal **882**, 34 (2019), ISSN 1538-4357, URL http://dx.doi.org/10.3847/1538-4357/ab2f73.

[26] W. Yuan, A. G. Riess, L. M. Macri, S. Casertano, and D. M. Scolnic, The Astrophysical Journal **886**, 61 (2019), ISSN 1538-4357, URL http://dx.doi.org/10.3847/1538-4357/ab4bc9.

[27] W. L. Freedman, B. F. Madore, T. Hoyt, I. S. Jang, R. Beaton, M. G. Lee, A. Monson, J. Neeley, and J. Rich, The Astrophysical Journal **891**, 57 (2020), ISSN 1538-4357, URL http://dx.doi.org/10.3847/1538-4357/ab7339.

[28] B. A. Robson, *Introductory chapter: Standard model of cosmology* (2019), URL https://www.intechopen.com/chapters/66783.

[29] J. L. Cervantes-Cota, G. Smoot, L. A. Ureña-López, H. A. Morales-Técotl, R. Linares-Romero, E. Santos-Rodríguez, and S. Estrada-Jiménez (2011), URL http://dx.doi.org/10.1063/1.3647524.

[30] *Lambda - parameters*, URL https://lambda.gsfc.nasa.gov/education/graphic_history/parameters.cfm.

[31] N. Aghanim, Y. Akrami, M. Ashdown, J. Aumont, C. Baccigalupi, M. Ballardini, A. J. Banday, R. B. Barreiro, N. Bartolo, and et al., Astronomy Astrophysics **641**, A6 (2020), ISSN 1432-0746, URL http://dx.doi.org/10.1051/0004-6361/201833910.

[32] K. T. Story, C. L. Reichardt, Z. Hou, R. Keisler, K. A. Aird, B. A. Benson, L. E. Bleem, J. E. Carlstrom, C. L. Chang, H.-M. Cho, et al., The Astrophysical Journal **779**, 86 (2013), ISSN 1538-4357, URL http://dx.doi.org/10.1088/0004-637X/779/1/86.

[33] P. A. R. Ade, N. Aghanim, C. Armitage-Caplan, M. Arnaud, M. Ashdown, F. Atrio-Barandela, J. Aumont, C. Baccigalupi, A. J. Banday, and et al., Astronomy Astrophysics **571**, A16 (2014), ISSN 1432-0746, URL http://dx.doi.org/10.1051/0004-6361/201321591.

[34] D. W. Hogg (1999), astro-ph/9905116.

[35] M. Richmond, *The angular diameter test*, URL http://spiff.rit.edu/classes/phys443/lectures/classic/classic.html.

[36] *Observations in cosmology*, URL https://ned.ipac.caltech.edu/level5/Peacock/Peacock3_4.html.

[37] G. Smoot, C. Bennett, A. Kogut, J. Aymon, C. Backus, G. de Amici, K. Galuk, P. Jackson, P. Keegstra, L. Rokke, et al., Advances in Space Research **11**, 193 (1991), ISSN 0273-1177, URL https://www.sciencedirect.com/science/article/pii/027311779190490B.

[38] J. M. Kovac, E. M. Leitch, C. Pryke, J. E. Carlstrom, N. W. Halverson, and W. L. Holzapfel, Nature **420**, 772–787 (2002), ISSN 1476-4687, URL http://dx.doi.org/10.1038/nature01269.

[39] W. Hu and M. White, *The cosmic symphony* (2004), URL http://background.uchicago.edu/~whu/Papers/HuWhi04.pdf.

[40] W. Hu, *Electric and magnetic modes*, URL http://background.uchicago.edu/~whu/polar/webversion/node8.html.

[41] *Planck power spectrum*, URL https://www.esa.int/ESA_Multimedia/Images/2013/03/Planck_Power_Spectrum.

[42] C. L. Bennett, M. Bay, M. Halpern, G. Hinshaw, C. Jackson, N. Jarosik, A. Kogut, M. Limon, S. S. Meyer, L. Page, et al., The Astrophysical Journal **583**, 1–23 (2003), ISSN 1538-4357, URL http://dx.doi.org/10.1086/345346.

[43] E. Komatsu, J. Dunkley, M. R. Nolta, C. L. Bennett, B. Gold, G. Hinshaw, N. Jarosik, D. Larson, M. Limon, L. Page, et al., The Astrophysical Journal Supplement Series **180**, 330–376 (2009), ISSN 1538-4365, URL http://dx.doi.org/10.1088/0067-0049/180/2/330.

[44] W. J. Percival, S. Cole, D. J. Eisenstein, R. C. Nichol, J. A. Peacock, A. C. Pope, and A. S. Szalay, Monthly Notices of the Royal Astronomical Society **381**, 1053–1066 (2007), ISSN 1365-2966, URL http://dx.doi.org/10.1111/j.1365-2966.2007.12268.x.

[45] N. Jarosik, C. L. Bennett, J. Dunkley, B. Gold, M. R. Greason, M. Halpern, R. S. Hill, G. Hinshaw, A. Kogut, E. Komatsu, et al., The Astrophysical Journal Supplement Series **192**, 14 (2011), ISSN 1538-4365, URL http://dx.doi.org/10.1088/0067-0049/192/2/14.

[46] W. J. Percival, B. A. Reid, D. J. Eisenstein, N. A. Bahcall, T. Budavari, J. A. Frieman, M. Fukugita, J. E. Gunn, Ivezić, G. R. Knapp, et al., Monthly Notices of the Royal Astronomical Society **401**, 2148–2168 (2010), ISSN 1365-2966, URL http://dx.doi.org/10.1111/j.1365-2966.2009.15812.x.

[47] A. G. Riess, L. Macri, S. Casertano, M. Sosey, H. Lampeitl, H. C. Ferguson, A. V. Filippenko, S. W. Jha, W. Li, R. Chornock, et al., The Astrophysical Journal **699**, 539–563 (2009), ISSN 1538-4357, URL http://dx.doi.org/10.1088/0004-637X/699/1/539.

[48] C. L. Bennett, D. Larson, J. L. Weiland, N. Jarosik, G. Hinshaw, N. Odegard, K. M. Smith, R. S. Hill, B. Gold, M. Halpern, et al., The Astrophysical Journal Supplement Series **208**, 20 (2013), ISSN 1538-4365, URL http://dx.doi.org/10.1088/0067-0049/208/2/20.

[49] P. A. R. Ade, N. Aghanim, M. I. R. Alves, C. Armitage-Caplan, M. Arnaud, M. Ashdown, F. Atrio-Barandela, J. Aumont, H. Aussel, and et al., Astronomy Astrophysics **571**, A1 (2014), ISSN 1432-0746, URL http://dx.doi.org/10.1051/0004-6361/201321529.

[50] A. Blanchard and J. Schneider, Astronomy and Astrophysics (1987).

[51] S. Mollerach, Physical Review D **57**, 1303–1305 (1998), ISSN 1089-4918, URL http://dx.doi.org/10.1103/PhysRevD.57.1303.

[52] D. Hanson, A. Challinor, and A. Lewis, General Relativity and Gravitation **42**, 2197–2218 (2010), ISSN 1572-9532, URL http://dx.doi.org/10.1007/s10714-010-1036-y.

[53] W. Hu, *Cmb as a physics laboratory*, URL https://slideplayer.com/slide/5092254/.

[54] G. Efstathiou, Monthly Notices of the Royal Astronomical Society **349**, 603–626 (2004), ISSN 1365-2966, URL http://dx.doi.org/10.1111/j.1365-2966.2004.07530.x.

[55] P. A. R. Ade, N. Aghanim, C. Armitage-Caplan, M. Arnaud, M. Ashdown, F. Atrio-Barandela, J. Aumont, C. Baccigalupi, A. J. Banday, and et al., Astronomy Astrophysics **571**, A15 (2014), ISSN 1432-0746, URL http://dx.doi.org/10.1051/0004-6361/201321573.

[56] P. A. R. Ade, N. Aghanim, M. Arnaud, M. Ashdown, J. Aumont, C. Baccigalupi, A. J. Banday, R. B. Barreiro, J. G. Bartlett, and et al., Astronomy Astrophysics **594**, A13 (2016), ISSN 1432-0746, URL http://dx.doi.org/10.1051/0004-6361/201525830.

[57] N. Aghanim, M. Arnaud, M. Ashdown, J. Aumont, C. Baccigalupi, A. J. Banday, R. B. Barreiro, J. G. Bartlett, N. Bartolo, and et al., Astronomy Astrophysics **594**, A11 (2016), ISSN 1432-0746, URL http://dx.doi.org/10.1051/0004-6361/201526926.

[58] R. J. Thornton, P. A. R. Ade, S. Aiola, F. E. Angilè, M. Amiri, J. A. Beall, D. T. Becker, H.-M. Cho, S. K. Choi, P. Corlies, et al., The Astrophysical Journal Supplement Series **227**, 21 (2016), ISSN 1538-4365, URL http://dx.doi.org/10.3847/1538-4365/227/2/21.

[59] S. K. Choi, M. Hasselfield, S.-P. P. Ho, B. Koopman, M. Lungu, M. H. Abitbol, G. E. Addison, P. A. R. Ade, S. Aiola, D. Alonso, et al., Journal of Cosmology and Astroparticle Physics **2020**, 045–045 (2020), ISSN 1475-7516, URL http://dx.doi.org/10.1088/1475-7516/2020/12/045.

[60] *South pole telescope (spt)*, URL https://lambda.gsfc.nasa.gov/product/spt/.

[61] J. W. Henning, J. T. Sayre, C. L. Reichardt, P. A. R. Ade, A. J. Anderson, J. E. Austermann, J. A. Beall, A. N. Bender, B. A. Benson, L. E. Bleem, et al., The Astrophysical Journal **852**, 97 (2018), ISSN 1538-4357, URL http://dx.doi.org/10.3847/1538-4357/aa9ff4.

[62] F. Bianchini, W. L. K. Wu, P. A. R. Ade, A. J. Anderson, J. E. Austermann, J. S. Avva, J. A. Beall, A. N. Bender, B. A. Benson, L. E. Bleem, et al., The Astrophysical Journal **888**, 119 (2020), ISSN 1538-4357, URL http://dx.doi.org/10.3847/1538-4357/ab6082.

[63] C. Blake and K. Glazebrook, The Astrophysical Journal **594**, 665–673 (2003), ISSN 1538-4357, URL http://dx.doi.org/10.1086/376983.

[64] W. J. Percival, R. C. Nichol, D. J. Eisenstein, D. H. Weinberg, M. Fukugita, A. C. Pope, D. P. Schneider, A. S. Szalay, M. S. Vogeley, I. Zehavi, et al., The Astrophysical Journal **657**, 51–55 (2007), ISSN 1538-4357, URL http://dx.doi.org/10.1086/510772.

[65] A. Heavens, R. Jimenez, and L. Verde, Physical Review Letters **113** (2014), ISSN 1079-7114, URL http://dx.doi.org/10.1103/PhysRevLett.113.241302.

[66] D. J. Eisenstein, W. Hu, and M. Tegmark, The Astrophysical Journal **504**, L57–L60 (1998), ISSN 0004-637X, URL http://dx.doi.org/10.1086/311582.

[67] D. Reid, URL https://ned.ipac.caltech.edu/level5/Sept02/Reid/Reid5_2.html.

[68] Aubourg, S. Bailey, J. E. Bautista, F. Beutler, V. Bhardwaj, D. Bizyaev, M. Blanton, M. Blomqvist, A. S. Bolton, J. Bovy, et al., Physical Review D **92** (2015), ISSN 1550-2368, URL http://dx.doi.org/10.1103/PhysRevD.92.123516.

[69] *The sloan digital sky survey: Mapping the universe*, URL https://www.sdss.org/.

[70] *The 2df galaxy redshift survey*, URL http://www.2dfgrs.net/.

[71] E. A. Kazin, J. Koda, C. Blake, N. Padmanabhan, S. Brough, M. Colless, C. Contreras, W. Couch, S. Croom, D. J. Croton, et al., Monthly Notices of the Royal Astronomical Society **441**, 3524–3542 (2014), ISSN 0035-8711, URL http://dx.doi.org/10.1093/mnras/stu778.

[72] D. J. Eisenstein, H. Seo, E. Sirko, and D. N. Spergel, The Astrophysical Journal **664**, 675–679 (2007), ISSN 1538-4357, URL http://dx.doi.org/10.1086/518712.

[73] D. Parkinson, S. Riemer-Sørensen, C. Blake, G. B. Poole, T. M. Davis, S. Brough, M. Colless, C. Contreras, W. Couch, S. Croom, et al., Physical Review D **86** (2012), ISSN 1550-2368, URL http://dx.doi.org/10.1103/PhysRevD.86.103518.

[74] K. S. Dawson, D. J. Schlegel, C. P. Ahn, S. F. Anderson, Aubourg, S. Bailey, R. H. Barkhouser, J. E. Bautista, A. Beifiori, A. A. Berlind, et al., The Astronomical Journal **145**, 10 (2012), ISSN 1538-3881, URL http://dx.doi.org/10.1088/0004-6256/145/1/10.

[75] D. Walsh, R. F. Carswell, and R. J. Weymann, Nature **279**, 381 (1979).

[76] S. Refsdal, Monthly Notices of the Royal Astronomical Society **128**, 307 (1964), ISSN 0035-8711, https://academic.oup.com/mnras/article-pdf/128/4/307/8073517/mnras128-0307.pdf, URL https://doi.org/10.1093/mnras/128.4.307.

[77] T. Treu and P. J. Marshall, The Astronomy and Astrophysics Review **24** (2016), ISSN 1432-0754, URL http://dx.doi.org/10.1007/s00159-016-0096-8.

[78] S. H. Suyu, V. Bonvin, F. Courbin, C. D. Fassnacht, C. E. Rusu, D. Sluse, T. Treu, K. C. Wong, M. W. Auger, X. Ding, et al., Monthly Notices of the Royal Astronomical Society **468**, 2590–2604 (2017), ISSN 1365-2966, URL http://dx.doi.org/10.1093/mnras/stx483.

[79] D. Paraficz and J. Hjorth, Astronomy Astrophysics **507**, L49–L52 (2009), ISSN 1432-0746, URL http://dx.doi.org/10.1051/0004-6361/200913307.

[80] I. Jee, E. Komatsu, and S. Suyu, Journal of Cosmology and Astroparticle Physics **2015**, 033 (2015), URL https://doi.org/10.1088/1475-7516/2015/11/033.

[81] I. Jee, E. Komatsu, S. Suyu, and D. Huterer, Journal of Cosmology and Astroparticle Physics **2016**, 031–031 (2016), ISSN 1475-7516, URL http://dx.doi.org/10.1088/1475-7516/2016/04/031.

[82] V. Bonvin, F. Courbin, S. H. Suyu, P. J. Marshall, C. E. Rusu, D. Sluse, M. Tewes, K. C. Wong, T. Collett, C. D. Fassnacht, et al., Monthly Notices of the Royal Astronomical Society **465**, 4914–4930 (2016), ISSN 1365-2966, URL http://dx.doi.org/10.1093/mnras/

stw3006.

[83] A. G. Riess, L. M. Macri, S. L. Hoffmann, D. Scolnic, S. Casertano, A. V. Filippenko, B. E. Tucker, M. J. Reid, D. O. Jones, J. M. Silverman, et al., The Astrophysical Journal **826**, 56 (2016), ISSN 1538-4357, URL http://dx.doi.org/10.3847/0004-637X/826/1/56.

[84] K. C. Wong, S. H. Suyu, G. C.-F. Chen, C. E. Rusu, M. Millon, D. Sluse, V. Bonvin, C. D. Fassnacht, S. Taubenberger, M. W. Auger, et al., Monthly Notices of the Royal Astronomical Society **498**, 1420–1439 (2019), ISSN 1365-2966, URL http://dx.doi.org/10.1093/mnras/stz3094.

[85] W. L. Freedman, *Measurements of the hubble constant: Tensions in perspective* (2021), 2106.15656.

[86] K. B. W. McQuinn, M. Boyer, E. D. Skillman, and A. E. Dolphin, The Astrophysical Journal **880**, 63 (2019), URL https://doi.org/10.3847/1538-4357/ab2627.

[87] R. Pogge, *Lecture 16: The evolution of low-mass stars*, URL http://www.astronomy.ohio-state.edu/~pogge/Ast162/Unit2/lowmass.html.

[88] A. G. Riess, W. Yuan, S. Casertano, L. M. Macri, and D. Scolnic, The Astrophysical Journal **896**, L43 (2020), ISSN 2041-8213, URL http://dx.doi.org/10.3847/2041-8213/ab9900.

[89] C. Feinstein, G. Baume, J. Rodriguez, and M. Vergne, *Extragalactic stellar photometry and the blending problem* (2019), 1903.10989.

[90] B. J. Mochejska, L. M. Macri, D. D. Sasselov, and K. Z. Stanek (2001), astro-ph/0103440.

[91] I. S. Jang, T. J. Hoyt, R. L. Beaton, W. L. Freedman, B. F. Madore, M. G. Lee, J. R. Neeley, A. J. Monson, J. A. Rich, and M. Seibert, The Astrophysical Journal **906**, 125 (2021), ISSN 1538-4357, URL http://dx.doi.org/10.3847/1538-4357/abc8e9.

[92] D. G. Turner, *The scale of reddening for classical cepheid variables* (2016), 1603.02276.

[93] I. S. Jang, D. Hatt, R. L. Beaton, M. G. Lee, W. L. Freedman, B. F. Madore, T. J. Hoyt, A. J. Monson, J. A. Rich, V. Scowcroft, et al., The Astrophysical Journal **852**, 60 (2018), ISSN 1538-4357, URL http://dx.doi.org/10.3847/1538-4357/aa9d92.

[94] G. S. Da Costa and T. E. Armandroff, **100**, 162 (1990).

[95] E. Carretta and A. Bragaglia, Astron. Astrophys. **329**, 937 (1998), astro-ph/9708249.

[96] T. Davidge, Publications of the Astronomical Society of the Pacific **115**, 635–646 (2003), ISSN 1538-3873, URL http://dx.doi.org/10.1086/375389.

[97] P. Marigo, L. Girardi, A. Bressan, P. Rosenfield, B. Aringer, Y. Chen, M. Dussin, A. Nanni,

G. Pastorelli, T. S. Rodrigues, et al., Astrophys. J. **835**, 77 (2017), 1701.08510.

[98] K. Aylor, Z. Hou, L. Knox, K. T. Story, B. A. Benson, L. E. Bleem, J. E. Carlstrom, C. L. Chang, H.-M. Cho, R. Chown, et al., The Astrophysical Journal **850**, 101 (2017).

[99] G. E. Addison, Y. Huang, D. J. Watts, C. L. Bennett, M. Halpern, G. Hinshaw, and J. L. Weiland, The Astrophysical Journal **818**, 132 (2016), ISSN 1538-4357, URL http://dx.doi.org/10.3847/0004-637X/818/2/132.

[100] N. Aghanim, Y. Akrami, M. Ashdown, J. Aumont, C. Baccigalupi, M. Ballardini, A. J. Banday, R. B. Barreiro, N. Bartolo, and et al., Astronomy Astrophysics **607**, A95 (2017), ISSN 1432-0746, URL http://dx.doi.org/10.1051/0004-6361/201629504.